# Catalytic Conversion of $CO_2$ to Hydrocarbons

by

Oscar Oyola Rivera

A thesis submitted in partial fulfillment of the requirements for the degree of

**MASTER of SCIENCE**

**in**

**CHEMICAL ENGINEERING**

UNIVERSITY OF PUERTO RICO
MAYAGÜEZ CAMPUS
2014

Approved by:

| | |
|---|---|
| Nelson Cardona Martínez, PhD<br>President, Graduate Committee | Date |
| María Martínez Iñesta, PhD<br>Member, Graduate Committee | Date |
| María Curet Arana, PhD<br>Member, Graduate Committee | Date |
| Aldo Acevedo Rullán, PhD<br>Chairperson of the Department | Date |
| Luis Rivera Montalvo, PhD<br>Graduate School Representative | Date |

## DEDICATION

This work is dedicated

to my parents
**Victor Oscar** and **Nivia Luz**,
who raised me to be the person I am today,

to my brother and nephews,
**Victor, Victor Armando** and **Paola**,

and my dog **Pirulo**

and to all those who accompanied me during this time.

**ACKNOWLEDGMENTS**

First of all, I wish to express my gratitude to my thesis advisor Dr. Nelson Cardona Martínez for his significant guidance, continuous encouragement, and all the valuable discussions that have helped in my development as research engineer and chemical scientist. I want to thank also to all the members of my thesis committee: Dr. María Martínez Iñesta and Dr. María Curet Arana for offering their assistance when needed and for providing access to their labs and instrumentation. I also wish to acknowledge the help and technical knowledge that I received from Mr. Angel Zapata during the installation and repair of various laboratory equipment and utilities.

I want to thank also to all my lab mates from Dr. Cardona Martínez research group; to Mrs. Darlene Galloza, Mr. Damian Reyes, and Mr. Christian Rivera for their assistance and valuable discussions, help and support.

In addition, I wish to thank the funding agency that make this work possible; to the National

Science Foundation (NSF) Partnership for Research and Education in Materials (PREM) Award DMR-0934115.

# ABSTRACT

The production of methanol and dimethyl ether via $CO_2$ hydrogenation was studied using Pd catalysts supported on α-$Ga_2O_3$, α-β-$Ga_2O_3$ and β-$Ga_2O_3$ polymorphs. The catalytic activity improves with the increase in the content of $Pd_2Ga$ intermetallic compound over the surface. The content of $Pd_2Ga$ over Pd/$Ga_2O_3$, reduced at 573 K, depends on the $Ga_2O_3$ crystalline phase present on the catalyst. A slight catalytic deactivation with time on stream was observed. The catalyst supported over α-β-$Ga_2O_3$ displayed the largest deactivation. The deactivation of the material appears to be the result of a loss of basic sites over the catalysts surface. The selectivity to dimethyl ether is not dependent on the $Pd_2Ga$ content, but depends on the catalyst acidity. The content of $Pd_2Ga$ over Pd/$Ga_2O_3$ catalysts was identified to be a crucial parameter for $CO_2$ hydrogenation to methanol and dimethyl ether.

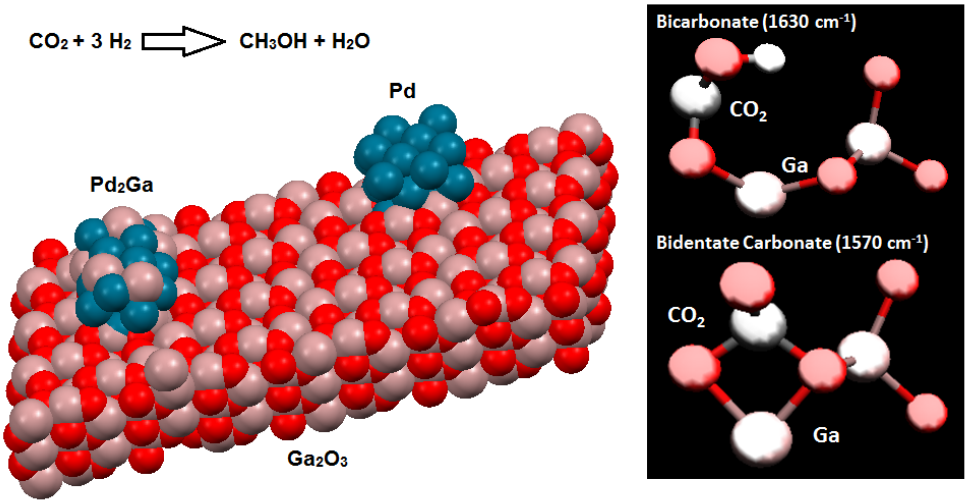

# RESUMEN

Se estudió la producción de metanol y éter dimetílico a través de la hidrogenación de $CO_2$ utilizando catalizadores de Pd soportados sobre α-$Ga_2O_3$, α-β-$Ga_2O_3$ y β-$Ga_2O_3$. La actividad catalítica mejora con el aumento en el contenido del compuesto intermetálico $Pd_2Ga$ sobre la superficie. El contenido de $Pd_2Ga$ sobre los catalizadores de Pd/$Ga_2O_3$, reducidos a 573 K, depende del polimorfo de $Ga_2O_3$ presente en el catalizador. Se observó una desactivación catalítica leve con el tiempo en flujo. La desactivación aparenta ser mayor sobre el catalizador con soporte α-β-$Ga_2O_3$. La desactivación del material parece ser resultado de una pérdida de lugares básicos sobre la superficie de los catalizadores. La selectividad al éter dimetílico es independiente del contenido de $Pd_2Ga$, pero depende de la acidez del catalizador. Se identificó que el contenido de $Pd_2Ga$ sobre catalizadores Pd/$Ga_2O_3$ puede ser un parámetro crucial para la hidrogenación de $CO_2$ a metanol y éter de dimetílico.

# TABLE of CONTENTS

# LIST of FIGURES

# LIST of TABLES

# *Chapter 1*

## 1. Introductory Remarks

The role of a catalyst is to accelerate a chemical reaction. A catalytic reaction can be described as a cyclic event in which the catalyst participates and is recovered in its original form at the end of the cycle [1]. The catalysts are divided into two main groups, homogeneous and heterogeneous catalysts. Heterogeneous catalysts accelerate a chemical reaction by chemically adsorbing reacting molecules, allowing these to react on the surface forming a product which is desorbed recycling the catalyst unaltered and allowing to be available for another reaction event [1,2].

The catalyst performance depends on the chemical and physical properties of the material. The surface area, adsorption properties, acidity and basicity have a strong influence on the material performance. The adsorption properties of the material are influenced by the acidity and basicity of the catalyst, making this selective to adsorb certain reacting molecules [3]. Heterogeneous catalysts with acidic and basic properties are mostly composed of metal oxides [4]. Many metal supported catalysts are bi-functional catalysts composed of transition metals and metal oxides [5].

This chapter pretends to give an introduction and description on the catalysts used during this work. The specific application of carbon dioxide hydrogenation and its importance will also be discussed. The motivation and an overview of this work is also presented.

## 1.1 $CO_2$ Hydrogenation

More than six and a half billion people burn fuels to provide electricity to their homes and industry, cook, keep warm, and to move about using cars, buses, boats, trains, and airplanes [6]. The burning of fuels produces carbon dioxide, which is released to the atmosphere. Carbon dioxide concentrations in the atmosphere have risen about 31% since industrial revolution period (1870) [6]. Carbon dioxide is a greenhouse gas, and the increased concentration of carbon dioxide in the atmosphere influences earth's radiation balance [6].

Hydrocarbons, such as methane, methanol and dimethyl ether, are potential alternative fuels that may be produced from $CO_2$ [7–9]. This is an important approach to reduce $CO_2$ emissions. To complete the $CO_2$ hydrogenation is necessary the presence of a bi-functional material. This material must have basic properties for the adsorption of $CO_2$, such as a metal oxide; and a species capable of adsorbing hydrogen dissociatively such as a transition metal. It is for this reason that catalysts with Cu-ZnO and Pd-$Ga_2O_3$ combinations are the most used materials for the hydrogenation of $CO_2$, the ZnO and $Ga_2O_3$ are responsible for the adsorption of $CO_2$, while Pd and Cu are responsible for the dissociative adsorption of $H_2$ [7,10–14]. Previous research showed that with the adequate combination of two metal species on a catalyst, the activity and selectivity to hydrogenation products from $CO_2$ is improved.

## 1.2 Pd supported on $Ga_2O_3$ catalysts

Palladium supported over gallium oxide has become a prominent catalyst for steam reforming and dehydrogenation of methanol [15–17], dehydrogenation of ethanol [18] and carbon dioxide hydrogenation to methanol [8,19–21].

The gallium oxide polymorphism and stability was studied by Roy and co-workers in 1952 [22]. All gallia polymorphs can be converted to the β form at high temperatures, making this phase the only stable thermodynamically one. As the names imply, the difference between the forms of $Ga_2O_3$ is its crystallographic structure. The β form has a monoclinic structure [22–24], while the α has a hexagonal corundum structure [22,25]. Figure 1 shows the unit cells for α-$Ga_2O_3$ and β-$Ga_2O_3$.

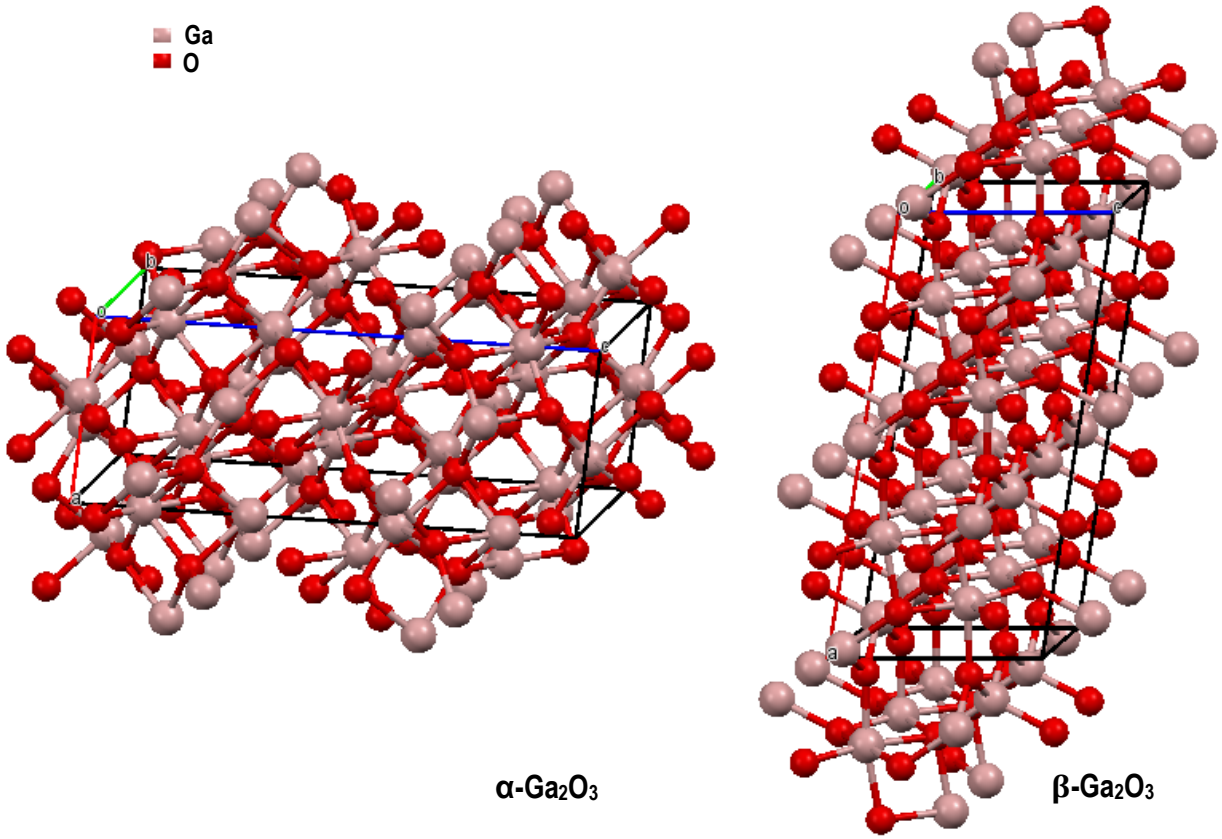


**Figure 1.** α-$Ga_2O_3$ and β-$Ga_2O_3$ unit cells.

Iwasa and co-workers, observed the formation of an intermetallic compound between palladium and gallium over Pd/$Ga_2O_3$ catalysts, which modifies the catalytic properties of the material for steam reforming and dehydrogenation of methanol [15,16]. It has been

demonstrated that the formation and the ratio of Pd and Ga in this intermetallic compound over the $Ga_2O_3$ surface depends on the reduction conditions [9,26]. The different Pd-Ga compounds exhibit a similar orthorhombic structures with Pbnm space group [27–29].

Fujitani and co-workers were the first to report the use of a $Pd/Ga_2O_3$ catalyst for the hydrogenation of $CO_2$ to methanol as an alternative to Cu/ZnO catalyst [8]. Bonivardi and co-workers demonstrated that the deposition of $Ga_2O_3$ over $Pd/SiO_2$ catalysts significantly enhances the catalytic activity for $CO_2$ hydrogenation to methanol [30]. They suggested that hydrogenation intermediates involved in methanol synthesis from $CO_2$, are similar over $Pd/Ga_2O_3$ and Cu/ZnO [30–34]. On the other hand, Li and co-workers demonstrated that the formation of a Pd-Ga intermetallic compound over $Pd/Ga_2O_3$ catalyst increases the catalytic performance for $CO_2$ hydrogenation to methanol [9].

One of the targets of this work is to find the $Ga_2O_3$ crystalline phase with better catalytic properties and explain the effect of this phase on $CO_2$ hydrogenation. Another goal is to explain the effect of $Pd_2Ga$ on $CO_2$ hydrogenation.

Results of this work show that catalysts with Pd and $Ga_2O_3$ have a higher performance than the catalysts with Cu and ZnO. Moreover, we showed that the deposition of Pd over $Ga_2O_3$ increases the performance compared with catalysts of $Pd\text{-}Ga_2O_3$ supported on $SiO_2$. The effect of the gallia polymorphism was also studied. The results showed that the polymorphism has an effect on the $CO_2$ adsorption and hydrogenation. Also this has an effect on the amount of $Pd_2Ga$ which is formed on the surface of the material. The results also show that with the increase in the content of $Pd_2Ga$ on the surface the overall activity of the catalyst increases.

## 1.3 Objectives

The goals of this study include:

- Comparison of the catalytic performance of Pd-$Ga_2O_3$ catalysts versus Cu-ZnO catalysts

- Synthesis and characterization using Nitrogen adsorption, X-ray diffraction, Fourier transform spectroscopy and transmission electron microscopy of α, α-β, β $Ga_2O_3$ crystallographic phases

- Synthesis and characterization using Nitrogen, Hydrogen and $CO_2$ adsorption; X-ray diffraction, Fourier transform spectroscopy and X-ray photoelectron spectroscopy of Pd supported on $Ga_2O_3$ polymorphs

- Comparison of the catalytic properties and performance of Pd/α-$Ga_2O_3$, Pd/α-β-$Ga_2O_3$ and Pd/β-$Ga_2O_3$

# *Chapter 2*

## 2. Methodology

### 2.1 Reaction System

The reactions are carried out in a packed bed flow reactor with an inline gas chromatograph equipped with a mass selective detector. The reaction system is detailed in Figure 2. It consists of four gas mass flow controllers (Brooks 5850E Series) controlled by a set-point controller (Brooks 0254), the packed bed reactor and a back pressure regulator (Tescom 26-1725-24), which controls the system pressure. The heating of the reactor is achieved by a heating tape, while control is performed by a PID controller (Omega CN-7800) connected with a solid state relay (Omega SSRL2400C10). The temperature is measured with a 1/16 inches diameter Type K thermocouple (Omega CASS-116U-12-NHX). The system has also four way valves (Whitey SS-43ZFS2), three way valves (Whithey SS-41XS2) and relief valves (Nupro SS-4R3A1-B). Helium, hydrogen and carbon dioxide gases are purified with gas purifiers specific for each one (VICI P-100-1 for He, P-200-1 for $H_2$, P-600-1 for $CO_2$), while the nitrogen is feed without any treatment.

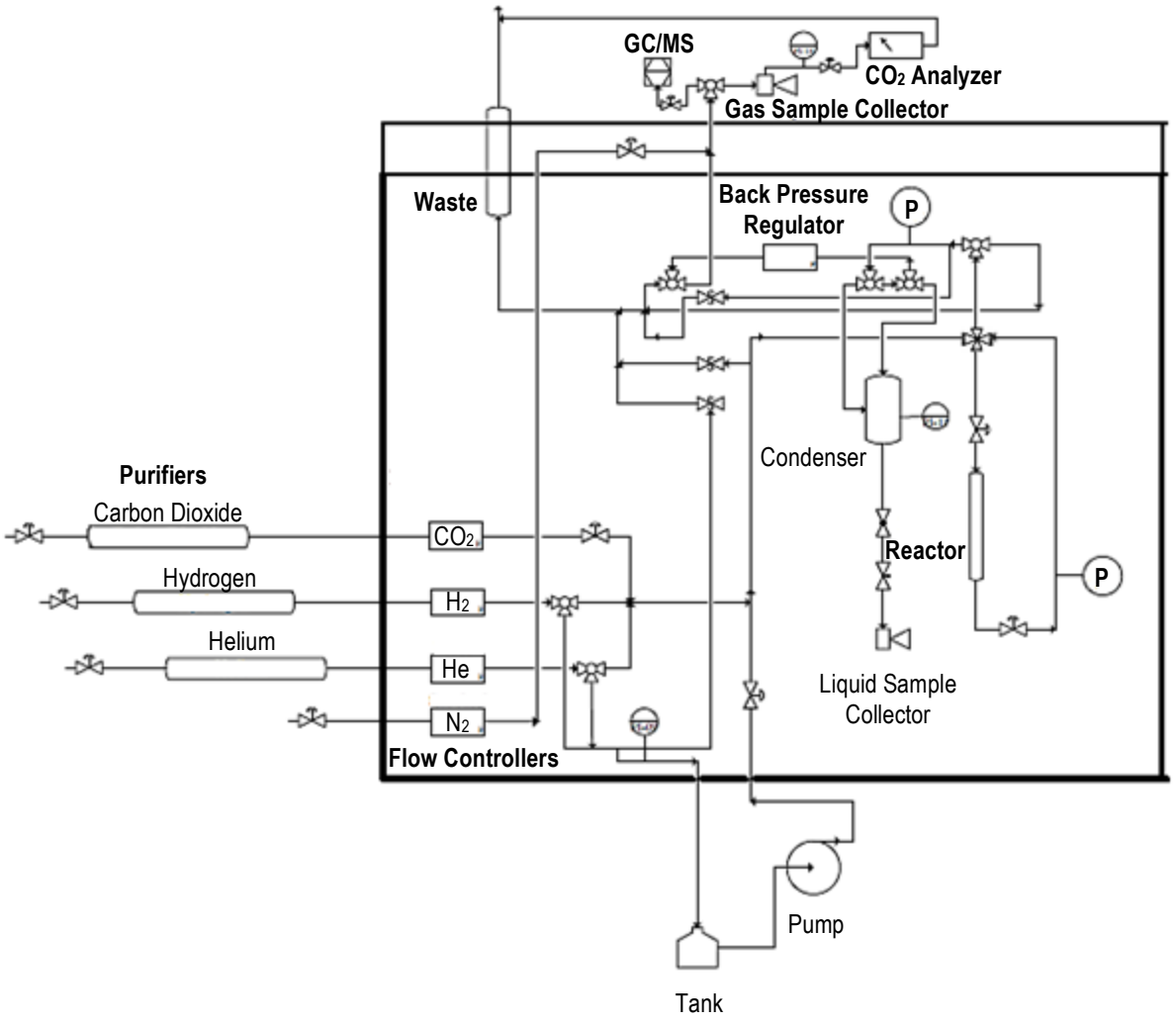


**Figure 2.** Reaction System.

## 2.2 Packed Bed Reactor

The packed bed reactor is detailed in Figure 3. The criteria for the experimental reactor design at laboratory scale are presented in Appendix A. The dimensions of the reactor are 17 cm of height and 0.50 cm of internal diameter. The reactor is packed vertically with three components: first quartz fiber as bed support with 5.5 cm of height, second the catalyst with

6 cm of height and finally Ottawa's sand to avoid temperature and flow variations when the gas is contacted with the catalyst.

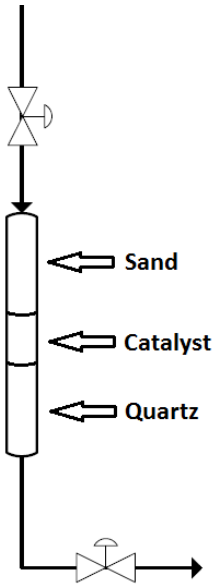


**Figure 3.** Packed Bed Reactor Assembly.

The reaction conditions are 543 K, 100-300 psig, 9-40 ml/min $CO_2$, 50-200 ml/min $H_2$ and 15 ml/min $N_2$. The weight hourly space velocity used were between 26.256 and 46.272 g reactants/h g catalyst. Before each reaction the sample is subjected to an *in-situ* reduction treatment at 543 K and atmospheric pressure with 15 ml/min $H_2$ and 135 ml/min He.

### 2.3 Products Analysis

The analysis of the products is performed using a gas chromatograph (*Hewlett-Packard* HP 6890) equipped with a mass selective detector (*Hewlett-Packard* 5973), using a 30 m capillary column (Agilent J&W 19091P-U04). The details of conditions, column and program used are summarized in Appendix B. The reagents and products are identified using a NIST

Mass Spectral Database v1.6B and retention indices obtained from literature. Nitrogen is used as an internal standard, the flow used was 15 ml/min. The peak areas collected from the GC/MS are referenced to the $N_2$ peak area.

The sampling station consists of a backpressure regulator (Tescom 26-2321-26), a 6 ports sampling valve (Valco) with a 250 µl loop, $CO_2$ analyzer (Quantek Instruments Model 906) and the GC/MS, mentioned above. The sampling station is detailed in Figure 4.

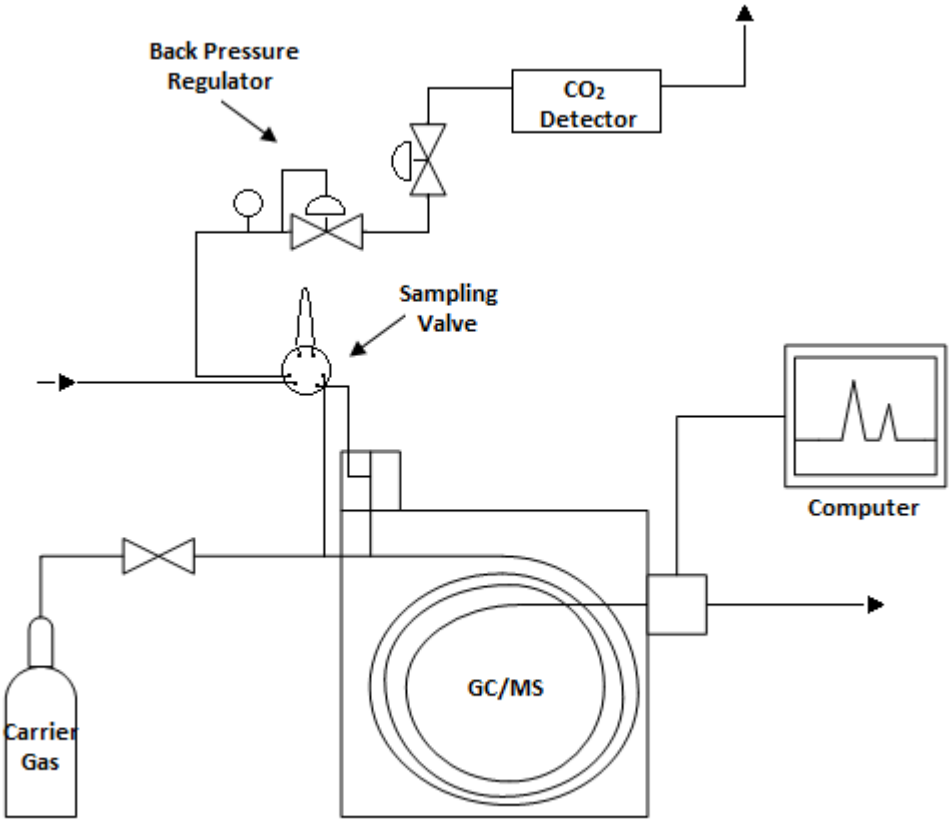


**Figure 4.** Sampling Station.

## 2.4 Characterization

### 2.4.1 Surface Area

The surface area analysis is carried out in an accelerated surface area and porosimetry system (Micromeritics ASAP 2020) using nitrogen (high purity grade, Linde) physisorption at liquid nitrogen temperature, 77 K. The surface area is calculated using the ASAP 2020 software and the BET method. The parameters and pretreatments conditions are detailed in Appendix C.

### 2.4.2 Active Metal Dispersion Analysis

The active metal dispersion analysis is also performed in the accelerated surface area and porosimetry system (Micromeritics ASAP 2020) using hydrogen (high purity grade, Praxair) or carbon monoxide (high purity grade, Praxair) depending on which metals are to be analyzed. The parameters and pretreatments conditions are detailed in Appendix C.

### 2.4.3 Crystall Structure Analysis

Crystal structure analysis was performed using an X-Ray diffractometer Rigaku Ultima III system equipped with cross beam optics and a $CuK_{\alpha}$ target operating at 40 kV and 44 mA. Standard diffraction patterns are gathered for 2θ angles ranging from 20 to $80^{o}$ at a scanning speed of $2^{o}$/min and a step size of $0.1^{o}$.

### 2.4.4 $Pd_2Ga$ Content Analysis

The Pd and $Pd_2Ga$ intermetallic compound contents over $Ga_2O_3$ polymorphs were calculated using X-ray photoelectron spectroscopy data between 330 eV and 350 eV. These

content were calculated based on Pd 3d 5/2 signals. The equipment used for this analysis was a PHI VersaProbe II Scaning XPS Microprobe unit.

### 2.4.5 $CO_2$ Adsorption

#### 2.4.5.1 $CO_2$ Adsorption

Carbon dioxide isotherms up to 0.85 MPa were measured at 308 K using an accelerated surface area and porosimetry system Micromeritics ASAP 2050 unit. For the determination of isosteric heat of $CO_2$ adsorption isotherms up to 0.11 MPa were measured at 308 K, 328 K and 348 K using an accelerated surface area and porosimetry system Micromeritics ASAP 2020 unit. Before the $CO_2$ uptakes were measured, each sample was pretreated at 543 K in $H_2$.

#### 2.4.5.2 FTIR $CO_2$ Adsorption

For the adsorption of $CO_2$ analysis using FTIR self-supported wafers of each sample were made by pressing 50 mg of powder at 7.2 metric tons. These wafers were placed in turn into a transmission infrared stainless steel cell with water-cooled $CaF_2$ windows, which was attached to a flow reactor system. Before each $CO_2$ adsorption experiment of, the catalysts were reduced *in-situ* with 10 % $H_2$ in $N_2$ at 543 K. An isothermal $CO_2$ adsorption-desorption experiment at 308 K and 0.4 MPa was carried out over each pretreated sample. Spectra were collected in the absorbance mode in a Fourier Transform Infrared Spectrometer Thermo Scientific Nicolet 6700.

### 2.4.6 Surface Acidity

The characterization of the type of acid sites over the catalysts surface was performed using pyridine adsorption. The adsorption of pyridine is performed over a 0.05 g sample disk with He saturated in pyridine for 1 h at atmospheric pressure and 473 K. The pyridine saturator is maintained at 273 K and He is flowed through the saturator. After the adsorption of the pyridine, the gas-phase and the reversible adsorbed pyridine is desorbed using 100 ml/min He at 473 K overnight. Then the sample is treated at 523, 573 and 623 K for 1 h at each temperature, taking a spectrum at each temperature including 473 K. The equipment for surface acidity characterization of the catalysts is a Fourier Transform Infrared Spectrometer (Thermo Scientific Nicolet 6700). The number of Lewis and Brønsted sites were calculated using the Beer-Lambert equation as described in Appendix E.

### 2.4.7 Scanning Electron Microscopy

Scanning electron microscopy (SEM) micrographs are obtained using a JEOL JSM-6390 system fitted with a SEI detector and a voltage of 10.0 kV. Energy-dispersive X-ray spectroscopy (EDS) is performed with an EDS Analysis System for SEM from EDAX Company.

## 2.5 Materials

We used tetraammine palladium (II) nitrate solution (5.0 wt% as Pd) from Strem Chemicals as metal precursor and gallium (III) nitrate hydrate 99.9998% from Acros Organics as the precursor for $Ga_2O_3$. A commercial catalyst support, $Ga_2O_3$ from Acros Organics, was used as a comparison, denominated as LS-$Ga_2O_3$ by the low surface area. Deionized (D.I.) water and 25 % Ammonium Hydroxide in water from Acros Organics were used as solvents. For catalytic

performance tests, the gases used include carbon dioxide (Food Grade, Praxair), hydrogen (High Purity, Praxair), helium (High Purity, Praxair) and nitrogen (Dry Grade, Praxair).

## 2.6 Experimental Procedure

### 2.6.1 Catalyst Preparation

To achieve the outlined objectives we started by screening different catalysts with different metals combinations, taking in consideration the most common combinations found in the literature. The catalysts were prepared using two methods of metal impregnation over a metal oxide support, these are incipient wetness impregnation using the procedure described by Chang [35] and evaporative deposition that basically is leaving the support with a solution of precursor with a greater volume than the total pore volume of the support at a low temperature until the solvent evaporates completely [36]. The detailed catalysts preparation is as follows:

1. The catalyst support is dried at 373 K in vacuum oven for 24 h, to remove the adsorbed water on the material. This support can be commercial or synthesized in our laboratory. The main supports used are $SiO_2$ and $Ga_2O_3$.
2. A solution with the metal precursor and deionized water is prepared using hydrated metal nitrates as the metal source. When the incipient wetness impregnation method is used the volume of the solution is equal to the total pore volume of the support sample. On the other hand, when the evaporative deposition method is used the volume of the solution is 40 mL. The metal species used were Pd, Ga, Cu and Zn. This solution only contains the first metal that will be impregnated.

3. The solution with the metal precursor is poured in an evaporating dish with the support. If the incipient wetness impregnation method is used the solution is poured drop wise with continuous manual stirring at room temperature. When the evaporative deposition method is used the metal precursor solution is poured completely in the evaporating dish with the support at 40$^{o}$C and stirred at 250 rpm until the solvent is completely evaporated.
4. After the deposition the material is dried at 313 K in vacuum for 24 h.
5. If we want to add another metal species the whole procedure is repeated from step 2 to step 4, for each metal.
6. The dry material is calcined at 673 K for 6 h with air to decompose the precursor and form the metal oxides over the surface.
7. The final step is the reduction of the material at 573 K for 6 h with $H_2$.

Two silicon dioxide supports were used $SiO_2$ (Aerosil200, Degussa) and SBA-15. The SBA-15 is synthesized following the procedure reported by Stucky and co-workers [37]. The α, α-β and β $Ga_2O_3$ crystalline phases were synthesized using the procedure reported by Wang and co-workers [38]. Two main solutions were prepared in D.I. water, one with 10 wt% gallium precursor and another with 5 wt% ammonium hydroxide. These two solutions were mixed in a drop wise manner under vigorous stirring until the pH value reached approximately 9. The white precipitate was filtered, washed with distillated water, and dried at 353 K in air to obtain the $Ga_2O_3$ precursor. The precursor was calcined at 673 K for 5 h in air to obtain α-$Ga_2O_3$. α-β-$Ga_2O_3$ and β-$Ga_2O_3$ were obtained by calcining α-$Ga_2O_3$ in air at 863 K and 1073 K, respectively.

### 2.6.2 Conversion of $CO_2$

Before each reaction, the reaction system is purged overnight with 50 ml/min He at room temperature and atmospheric pressure. After the reaction system is purged, the reactor is packed with quartz fiber, catalyst (sieve 40-50) and an inert solid (Ottawa sand). Catalyst samples were pressed into wafers at 10,000 psi of pressure, milled using mortar and pestle and finally sieved to obtain particles between 0.420 and 0.297 mm of diameter (sieve 40-50). About 0.5 g were weighed and placed in the reactor.

The catalysts are reduced *in situ* at 543 K and atmospheric pressure with 15 ml/min $H_2$ and 135 ml/min He for 2 hours. After the reduction the system is pressurized up to 250 psig with He. The sampling area is pressurized at 20 psig and heated at 353 K to avoid changes in the temperature and accumulation of methanol in the lines.

The reactants are fed to the system with the reactor isolated, until the $CO_2$ concentration measured with the $CO_2$ meter is stabilized, then a sample of the reaction mixture is analyzed in the GC/MS providing the feed concentration of $CO_2$.

The reactants are then passed through the reactor with the desired proportions. The first sample is taken after 12 min, then samples are taken every hour until the reaction reaches steady state. To finish the reaction the reactor is isolated and cooled. Another sample of the reactive mixture is taken when the $CO_2$ composition is stabilized again at the end of the reaction to confirm the feed concentration.

## 2.7 Catalytic Performance Calculations

The two main reactions studied are the hydrogenation of $CO_2$ to methanol and the conversion of methanol to dimethyl ether.

$$CO_2 + 3\ H_2 \rightleftarrows CH_3OH + H_2O \qquad \text{(Eq. 1)}$$

$$2\ CH_3OH \rightleftarrows CH_3OCH_3 + H_2O \qquad \text{(Eq. 2)}$$

The GC/MS allows the measurement of $CO_2$ and products concentrations. The peak area are divided by the internal standard ($N_2$) peak area to correct for the variations that can occur due to changes in pressure or temperature. To quantify the results we prepared calibration curves using standards. The molar flows of any reactant or product are calculated using the linear regression of the appropriate curve. With these molar flows, the conversion, yield and selectivity for the different catalysts are calculated. The conversion of the catalysts is calculated using the $CO_2$ molar flow compiled from the GC/MS calibration curve for $CO_2$.

$$X_{CO2} = \frac{F_{CO2,in} - F_{CO2,out}}{F_{CO2,in}} * 100 \qquad \text{(Eq. 3)}$$

where $F_{CO2,in}$ is the initial molar flow of $CO_2$, $F_{CO2,out}$ the molar flow of $CO_2$ at time on stream **t** of reaction and $X_{CO2}$ is the $CO_2$ conversion percent [%].

The catalyst yields and selectivity are calculated using the products and carbon dioxide molar flows. To calculate the yield of the catalyst to produce a specific product we use the product and the carbon dioxide feed and exit flows.

$$Y_p = \frac{F_p}{(F_{CO2,in} - F_{CO2,out}) * \eta_P} * 100 \qquad \text{(Eq. 4)}$$

where $F_p$ is products molar flow, $F_{CO2,in}$ is the initial $CO_2$ molar flow, $F_{CO2,out}$ is the $CO_2$ molar flow at time on stream **t** of reaction, $\eta_P$ the product stoichiometric number and $Y_p$ is the yield percent of the catalyst to produce a specific product [%].

The selectivity of the catalysts is calculated using the product species of interest molar flow over the molar flow of all products.

$$S_{pi} = \frac{F_{pi}}{F_p} * 100 \qquad \text{(Eq. 5)}$$

where $F_{pi}$ is the product of interest molar flow, $F_p$ is the products molar flow and $S_{p1}$ is the catalyst selectivity percent for product of interest (p1).

The turn over frequency (TOF) was calculated based on the moles of $CO_2$ consumed over time and the total metal sites on the catalyst.

$$TOF = \frac{F_{CO2}^{o} - F_{CO2}^{f}}{n^{*}} \qquad \text{(Eq. 6)}$$

Where $F_{CO2}^{f}$ is the $CO_2$ outlet flow rate at steady state [mol/s], $F_{CO2}^{o}$ is the $CO_2$ inlet flow rate [mol/s] and $n^{*}$ is the number of metal sites.

The reaction rates are obtained using the reaction system as a differential reactor.

$$\frac{W}{F_{CO2}^{o}} = \frac{X_{CO2}}{-r_{CO2}} \qquad \text{(Eq. 7)}$$

Where $X_{CO2}$ is the $CO_2$ conversion percent [%] / 100, W is the Catalyst weight [g], $F^{o}_{CO2}$ is the $CO_2$ inlet flow rate [mol/s]and $r_{CO2}$ is $CO_2$ reaction rate [mol/s g]**.**

# *Chapter 3*

## 3. Characterization

### 3.1 Surface Area

Table 1 shows the BET surface area obtained for different fresh catalysts supported on $SiO_2$. The catalyst supported on SBA-15 has the highest surface area due to its mesoporous structure, while the $SiO_2$ is an amorphous fumed silica. The $Ga_2O_3$ polymorphs surface area decreases while the crystalline phase changes from α to β phase. This is the first signal of changes in structure.

**Table 1.** BET Surface Area for $SiO_2$ and $Ga_2O_3$ supported catalysts

| Catalyst | Metal wt%(*) | BET Surface Area ($m^2/g$) |
|---|---|---|
| $SiO_2$ | 0 | 196 |
| $Cu/SiO_2$ | 5 | 189 |
| $Cu\text{-}ZnO/SiO_2$ | 5.8 Cu<br>1.7 Zn | 164 |
| $Cu\text{-}ZnO\text{-}Ga_2O_3/SiO_2$ | 7 Cu<br>2.1 Zn<br>1.6 Ga | 160 |
| $Pd\text{-}Ga_2O_3/SiO_2$ | 1.5 Pd<br>2.5 Ga | 209 |
| $Pd\text{-}Ga_2O_3/SBA15$ | 1.6 Pd<br>2.3 Ga | 653 |
| $\alpha\text{-}Ga_2O_3$ | 0 | 62 |
| $\alpha\text{-}\beta\text{-}Ga_2O_3$ | 0 | 32 |
| $\beta\text{-}Ga_2O_3$ | 0 | 28 |
| $LS\text{-}Ga_2O_3$ | 0 | < 20 |
| $Pd/\alpha\text{-}Ga_2O_3$ | 3.9 | 38 |
| $Pd/\alpha\text{-}\beta\text{-}Ga_2O_3$ | 2.2 | 38 |
| $Pd/\beta\text{-}Ga_2O_3$ | 2 | 22 |
| $Pd/LS\text{-}Ga_2O_3$ | 2 | 27 |

**(*) Calculated using EDS**

### 3.2 Crystallographic Structures

To confirm the crystallographic structure changes for the $Ga_2O_3$ polymorphs XRD patterns where obtained, as shown in Figure 5. This figure shows the patterns for pure α and β phases of $Ga_2O_3$. This figure also shows the XRD pattern for a polycrystalline structure of $Ga_2O_3$ containing, mainly, α phase and a low concentration of the β phase. The low concentration of the β phase is due to the calcination temperature used to form this mixture, it was confirmed by Wang and co-workers that at 863 K the β phase begins to form obtaining a low β phase concentration [38]. It is claimed by the appearance of a characteristic peak of the β phase at $30.5^o$ 2θ, shown in insert B of Figure 5, and a change in the relative intensities for α phase characteristic peaks. The LS-$Ga_2O_3$ also shows the β phase.

XRD patterns for $SiO_2$ supported catalysts did not display peaks for crystalline Pd and $Ga_2O_3$. This result implies that the samples are amorphous or that the crystallite sizes are too small to be detected by the instrument used. Since our samples are calcined at 673 K we are assuming that $Ga_2O_3$ is in the α-$Ga_2O_3$ phase. Samples of $Ga_2O_3$ calcined at 673 K present the alpha phase.

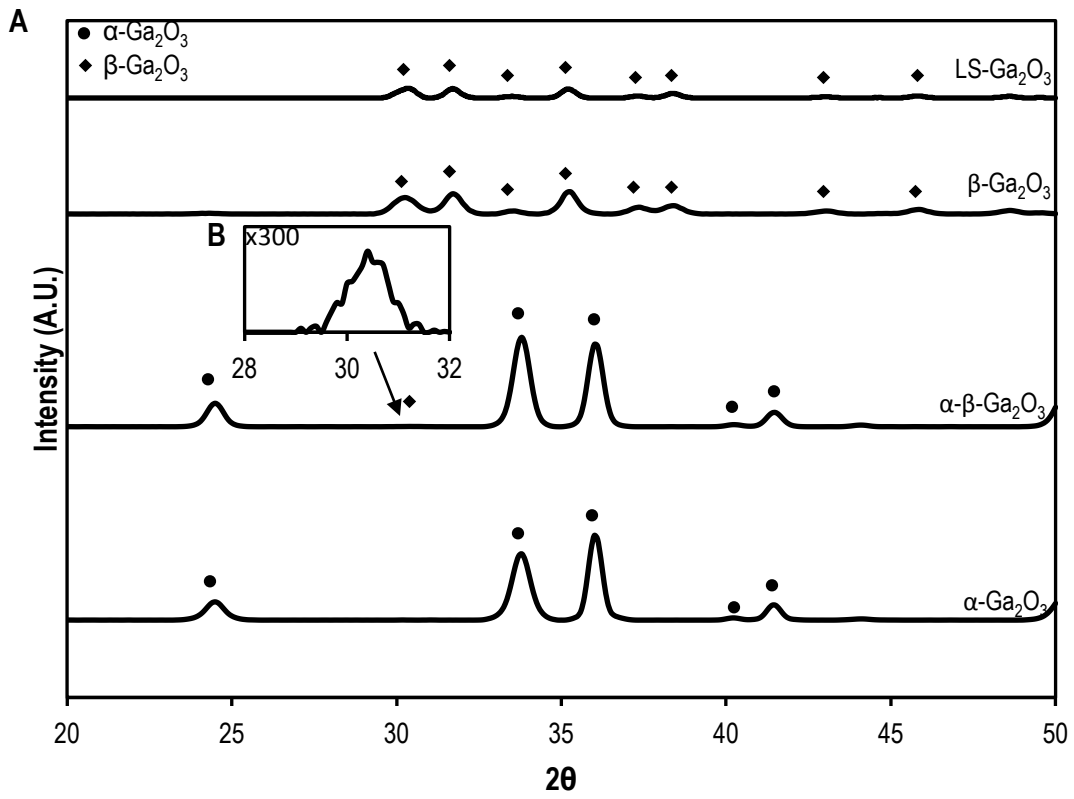


**Figure 5.** XRD patterns for $Ga_2O_3$ crystalline phases.

The formation of intermetallic $Pd_xGa$ over $Ga_2O_3$ polymorphs occurs depending on the reduction temperature at which the $Pd/Ga_2O_3$ catalyst is exposed, and the crystalline phase of the $Ga_2O_3$ polymorph [26,39]. All catalysts studied here were reduced at 573 K in $H_2$. The XRD patterns for Pd impregnated $Ga_2O_3$ polymorphs are shown in Figure 6. The XRD results are consistent with the formation of $Pd_2Ga$ species over $Pd/\beta\text{-}Ga_2O_3$ and $Pd/LS\text{-}Ga_2O_3$, according to the work of Haghofer and co-workers [26]. The appearance of two characteristic peaks for $Pd_2Ga$ at 39.6 and 40.3° for $Pd/\alpha\text{-}Ga_2O_3$ and $Pd/\alpha\text{-}\beta\text{-}Ga_2O_3$ also support the formation of $Pd_2Ga$ over these materials. A characteristic peak of $\alpha\text{-}Ga_2O_3$ that increases its intensity after Pd deposition overlaps the main characteristic peak of $Pd_2Ga$ in the pattern for $Pd/\alpha\text{-}Ga_2O_3$ and

Pd/α-β-$Ga_2O_3$. These results are consistent with those obtained by Lorenz and co-workers who observed the formation of $Pd_2Ga$ over α-$Ga_2O_3$ at the same reduction temperature [39].

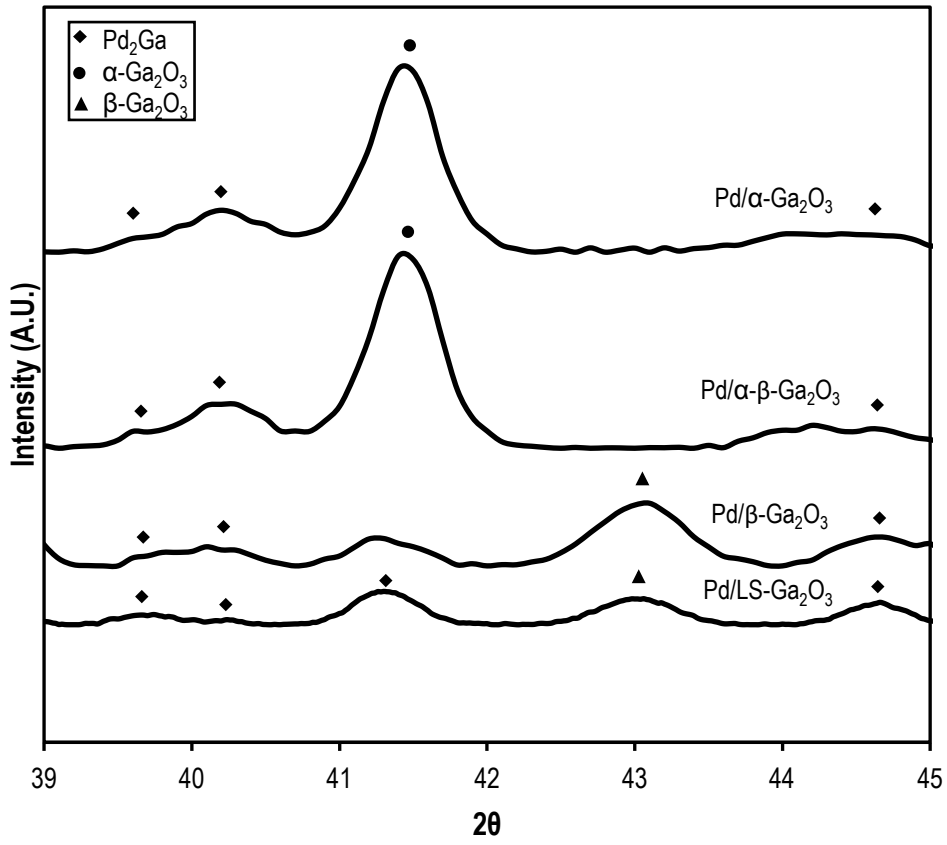


**Figure 6.** XRD patterns for $Pd_2Ga$ over Pd/$Ga_2O_3$ catalysts.

### 3.3 $Pd_2Ga$ content

The $Pd_2Ga$ content on the catalysts surface was determined by deconvoluting the XPS spectra for the catalysts. Figure 7 shows the deconvulated XPS spectra for the $Ga_2O_3$ supported catalysts. The XPS spectra for the Pd/$Ga_2O_3$ catalysts exhibit a shift in the Pd 3d 5/2 signal at 336.1 eV, shifted to higher binding energies compared to metallic Pd. This shift is attributed to the $Pd_2Ga$ formation over different $Ga_2O_3$ polymorphs [40]. Table 2 summarizes the Pd and

$Pd_2Ga$ contents over the different $Ga_2O_3$ polymorphs. The highest $Pd_2Ga$ content was obtained for samples containing the β-$Ga_2O_3$ crystalline phase, *i.e.*, Pd/β-$Ga_2O_3$ and Pd/LS-$Ga_2O_3$. The difference in $Pd_2Ga$ abundance over $Ga_2O_3$ polymorphs may depend on the $Ga_2O_3$ crystalline phase stability at 573 K under $H_2$, facilitating an induced reduction of the support by the spill of atomic hydrogen activated by Pd over the surface [9,41]. Table 2 also shows the quantity of metal sites over $Ga_2O_3$ polymorphs calculated from $H_2$ chemisorption isotherms at 308 K. The exposed metal sites per gram is lower on samples containing the β-$Ga_2O_3$ crystalline phase, *i.e.*, Pd/β-$Ga_2O_3$ and Pd/LS-$Ga_2O_3$, it is worth noting that the total metal content in these samples is also less. These results are consistent with the results obtained by XPS.

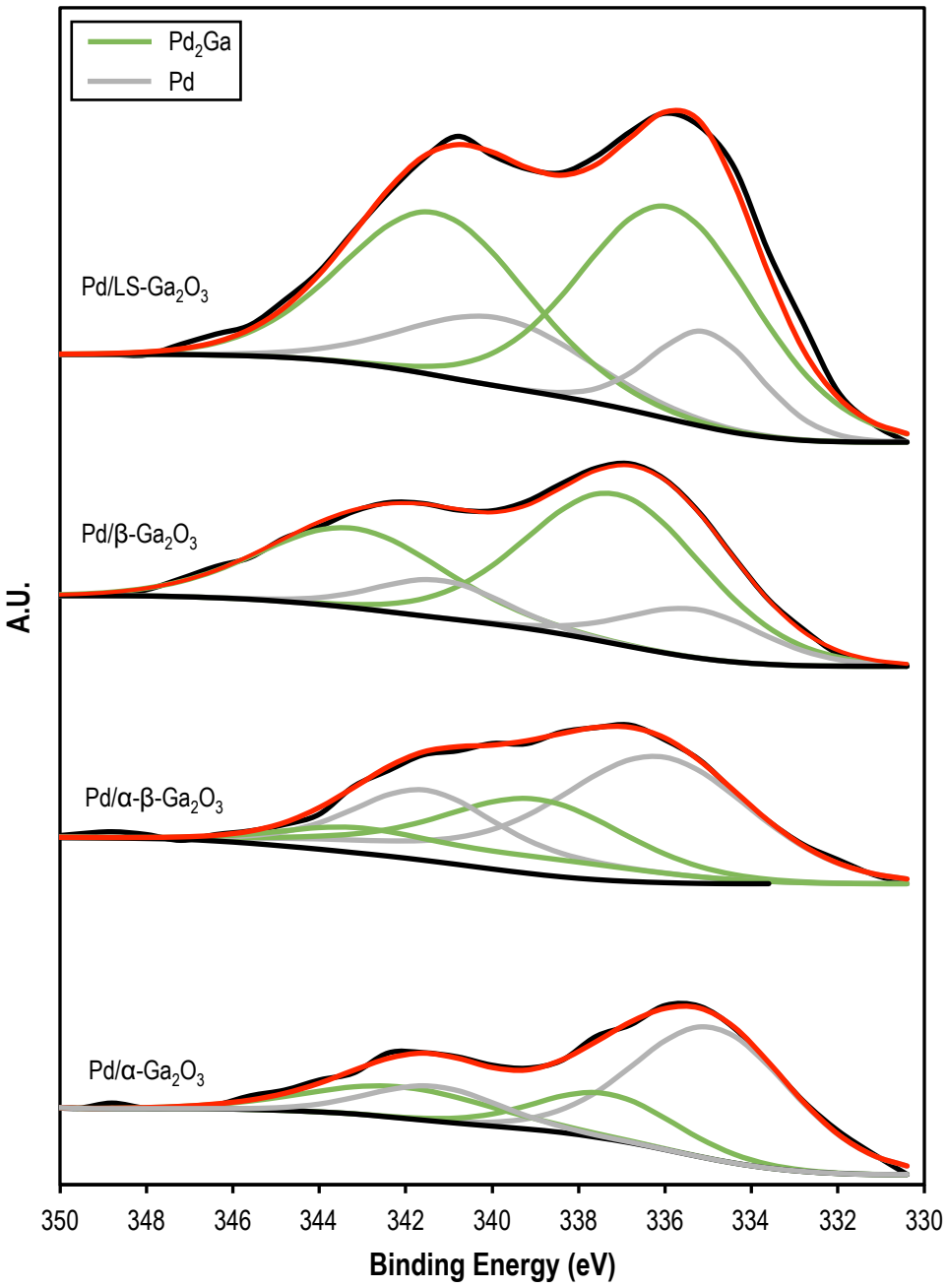


**Figure 7.** XPS spectra for Pd supported catalysts over $Ga_2O_3$ polymorphs.

**Table 2.** Pd and $Pd_2Ga$ content over $Ga_2O_3$ polymorphs

| Catalyst | [Pd] (%) | [$Pd_2Ga$] (%) | Metal Sites (mmol/g) |
|---|---|---|---|
| Pd/α-$Ga_2O_3$ | **67.43** (335.2 eV) | **32.57** (337.2 eV) | 0.063 |
| Pd/α-β-$Ga_2O_3$ | **70.97** (336.0 eV) | **29.03** (339.2 eV) | 0.067 |
| Pd/β-$Ga_2O_3$ | **21.71** (335.2 eV) | **78.29** (336.8 eV) | 0.002 |
| Pd/LS-$Ga_2O_3$ | **22.14** (335.2 eV) | **77.86** (336.1 eV) | 0.014 |

### 3.4 $CO_2$ adsorption

$CO_2$ adsorption isotherms from 0.01 MPa to 0.86 MPa at 308 K over Pd supported on $Ga_2O_3$ polymorphs were collected, as shown in Figure 8. The $CO_2$ uptake decreases as the surface area decreases, therefore it can be assumed that the adsorbed amount of $CO_2$ at 308 K depends on the surface area of $Ga_2O_3$ [42]. At low pressures between 0.01 MPa and 0.27 MPa the $CO_2$ adsorption appears to be greater over Pd/α-β-$Ga_2O_3$ with a small difference compared to Pd/α-$Ga_2O_3$, while at pressures above 0.27 MPa the adsorption is greater over Pd/α-$Ga_2O_3$.

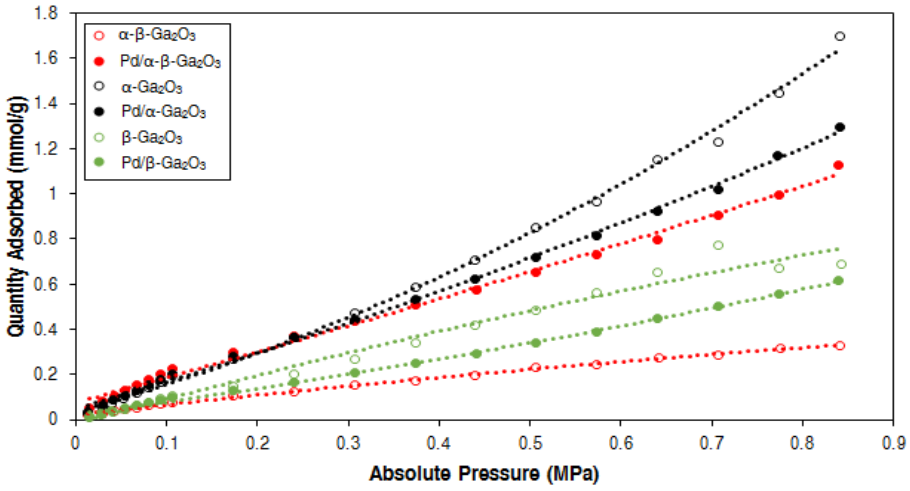


**Figure 8.** Adsorption isotherms for $CO_2$ adsorbed over $Ga_2O_3$ and Pd/$Ga_2O_3$ polymorphs.

FTIR spectra after $CO_2$ adsorption for Pd supported over $Ga_2O_3$ polymorphs were collected at 308 K and 0.34 MPa as shown in Figure 9. Two characteristic bands at 1630 and 1580 $cm^{-1}$ are observed for all samples that correspond to two low strength basic sites. The band at 1630 $cm^{-1}$ corresponds to $CO_2$ bonded as a bicarbonate and the band at 1580 $cm^{-1}$ corresponds to a $CO_2$ bonded as a bidentate carbonate over the catalysts surface [43,44]. The $CO_2$ adsorption properties change depending on the $Ga_2O_3$ polymorph present, the ratio of the peak area for carbonate bidentate and bicarbonate bands changes between phases. The ratio of the peak areas for these bands for the catalysts supported on β-$Ga_2O_3$ and LS-$Ga_2O_3$ that have the same crystal structure, are 1.1 and 0.8 respectively, as shown in Figure 10. The bidentate carbonate bond is stronger than the bicarbonate bond [44].

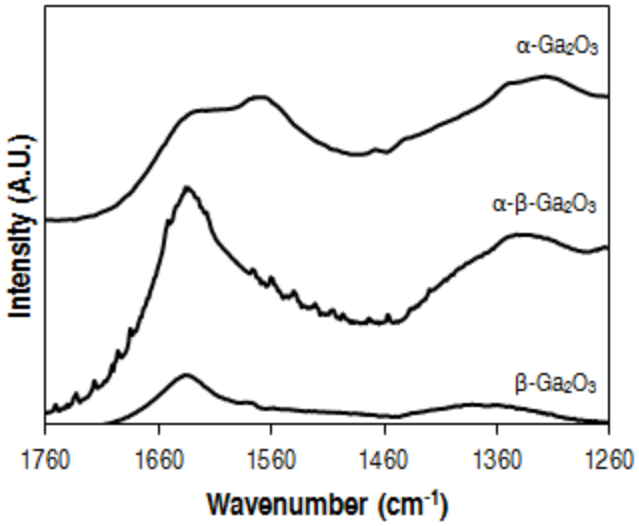


**Figure 9.** FTIR spectra for $CO_2$ adsorbed over $Pd/Ga_2O_3$ catalysts.

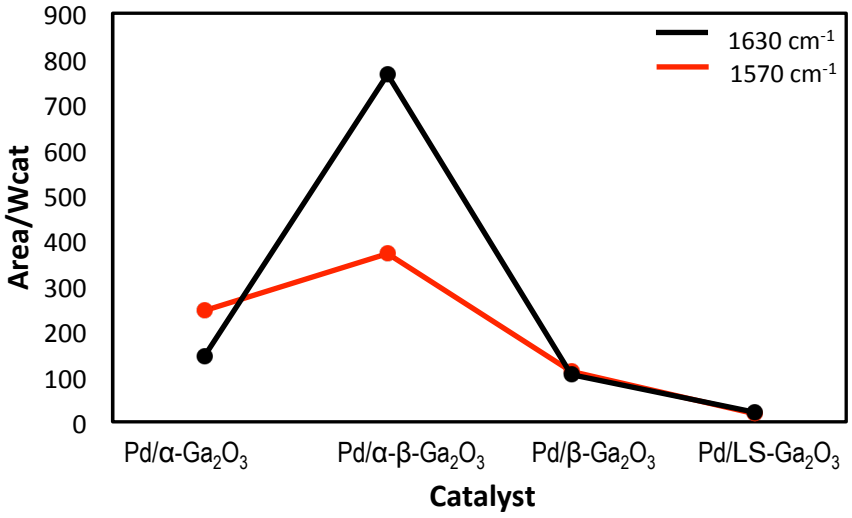


**Figure 10.** $CO_2$ adsorbed FTIR signal area for supported $Ga_2O_3$ polymorphs normalized by the sample mass.

FTIR spectra for $CO_2$ adsorption over $\alpha$-$Ga_2O_3$ at temperatures from 323 to 473 K were collected, as shown in Figure 11. These bands mentioned above, decrease in intensity with an

increase in temperature confirming a moderate interaction between the $CO_2$ molecule and the $Ga_2O_3$ basic sites, consistent with the work of Collins and co-workers [43].

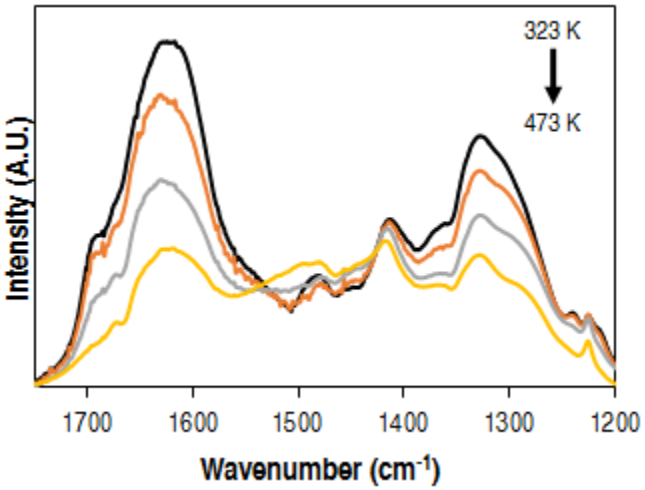


**Figure 11.** FTIR spectra for $CO_2$ adsorbed for α-$Ga_2O_3$ at temperatures from 323 to 473 K.

The isosteric heat of adsorption was calculated using the Clausius Clapeyron equation from adsorption data from 308 K to 348 K for Pd supported catalysts over $Ga_2O_3$ polymorphs, as shown in Table 3. The isosteric heat may be influenced by the $Ga_2O_3$ crystalline phase and the $Pd_2Ga$ content. The highest isosteric heat of adsorption was observed for the Pd/α-β-$Ga_2O_3$ catalyst that has the lowest $Pd_2Ga$ content. The small difference in the isosteric heat of adsorption for the Pd/α-$Ga_2O_3$ and Pd/β-$Ga_2O_3$ when compared to Pd/α-β-$Ga_2O_3$ catalyst may be due to the reduction of the number of basic sites on these catalysts by the formation of $Pd_2Ga$. The Pd/α-$Ga_2O_3$ and Pd/β-$Ga_2O_3$ catalysts has a higher content of $Pd_2Ga$ over the surface.

**Table 3.** Isosteric heat of $CO_2$ adsorption over Pd supported on $Ga_2O_3$ polymorphs

| Catalyst | $-\Delta H_{CO2}^{ads}$ (kJ/mol) |
|---|---|
| Pd/α-$Ga_2O_3$ | 17.2 |
| Pd/α-β-$Ga_2O_3$ | 21.6 |
| Pd/β-$Ga_2O_3$ | 15.3 |

### 3.5 Surface Acidity

The FTIR spectroscopy of adsorbed pyridine provides the type of acidity present on the catalysts. Figure 12 shows FTIR spectra for pyridine adsorbed on $SiO_2$ and SBA-15 supported catalysts. This figure shows the effect of adding $Ga_2O_3$ to $SiO_2$ catalysts. The catalyst without $Ga_2O_3$ does not present acid sites, only shows low intensity peaks corresponding to pyridine adsorbed by hydrogen bonds, while the catalysts with $Ga_2O_3$ show acid sites with characteristic bands at 1623, 1611, 1546, 1496 and 1458 $cm^{-1}$. The most abundant acidic sites over these surfaces are of Lewis type, but the ratio of Brønsted/Lewis acidic sites changes between $SiO_2$ and SBA-15 supported catalysts. The Brønsted/Lewis ratio dominates for the SBA-15 supported catalyst, with a Brønted/Lewis ratio of 0.17 compared to 0.13 in $SiO_2$ supported material this ratio is calculated using the bands at 1458 $cm^{-1}$ for Lewis sties and 1546 $cm^{-1}$ for Brønsted sites.

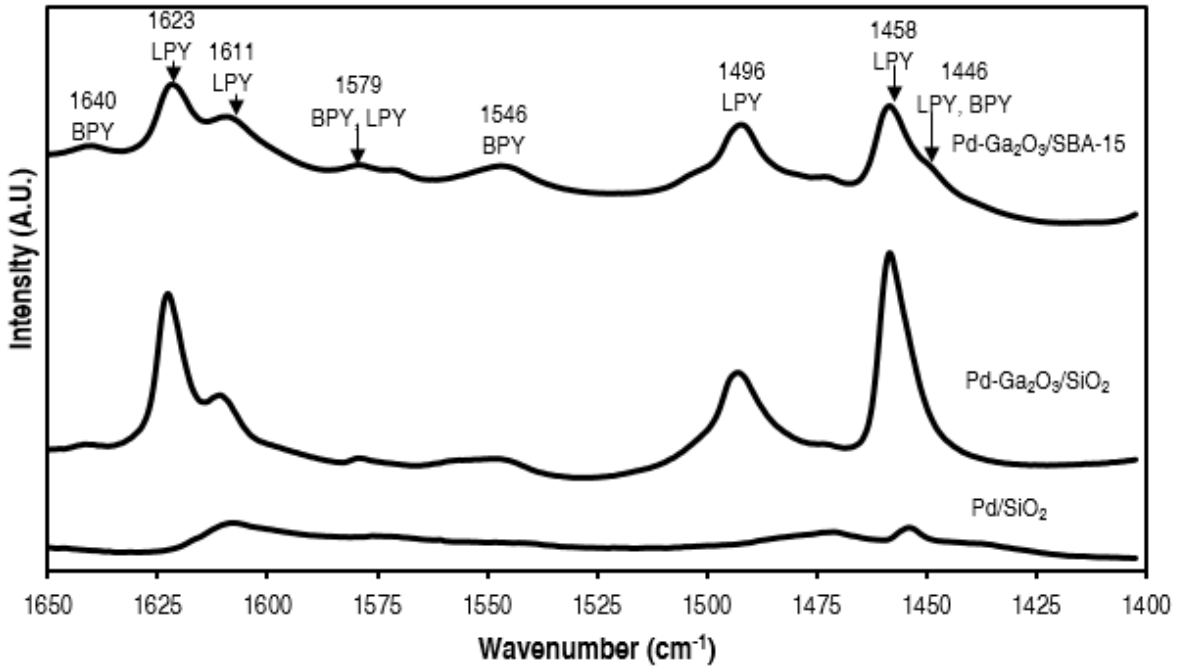


**Figure 12.** Pyridine adsorption FTIR spectra for $SiO_2$ supported catalysts at 473 K.

Figure 13 shows the FTIR spectra for pyridine adsorbed on different $Ga_2O_3$ crystalline phases. All the phases show the same types of acid sites but the acid sites abundance changes between phases. The LS-$Ga_2O_3$ has the lowest acidity, this could be related to the low surface area of this material. The acidity for the α, α-β and β phases changes between phases, decreasing form α to α-β and increasing from α-β to β phase. We do not observe evidence for Brønsted acidity for the $Ga_2O_3$ oxide samples. The appearance of these Brønsted sites on silica supported materials is due to Ga cation bonded tetrahedrally on silica surface, generating bridges between Ga and Si hydroxyl groups [45,46].

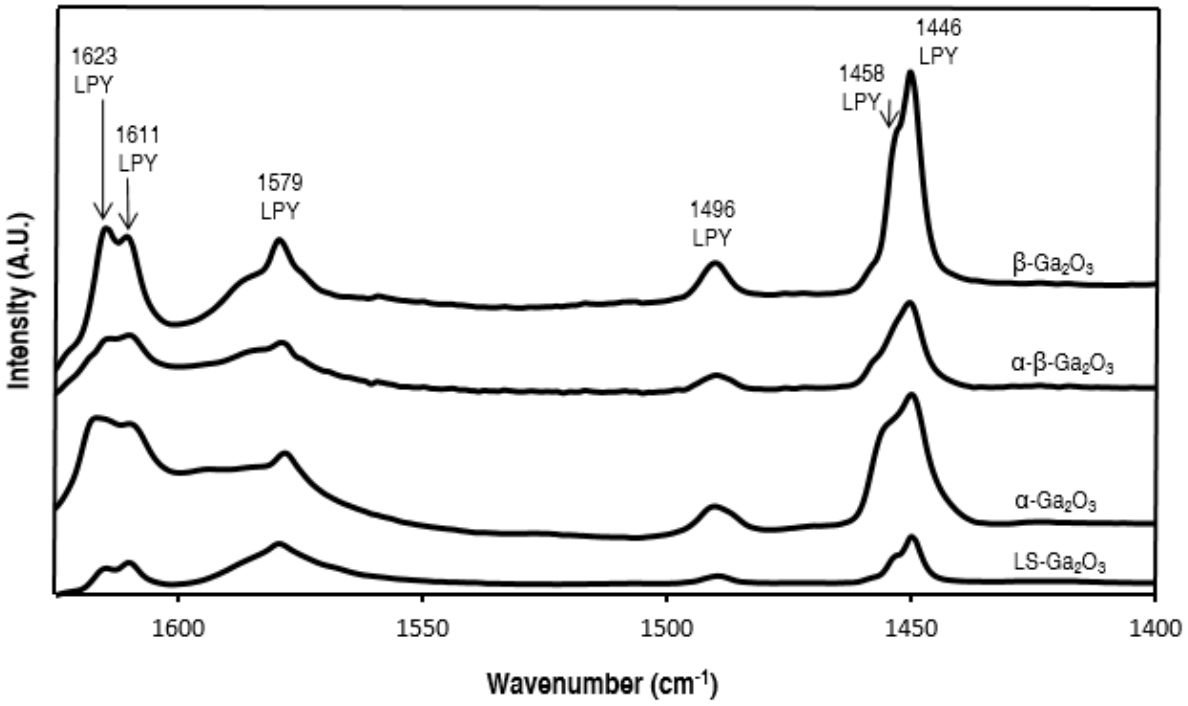


**Figure 13.** Pyridine adsorption FTIR spectra for $Ga_2O_3$ crystalline phases al 473 K.

Figure 14 shows the effect of adding Pd to $Ga_2O_3$ catalysts. The addition of Pd on $Ga_2O_3$ polymorphs causes the generation of Brønsted sites with characteristic bonds on 1549 and 1640 $cm^{-1}$. The appearance of these Brønsted sites on gallia supported materials is due to Pd cation bonded tetrahedrally on gallia surface, generating bridges between Ga hydroxyl groups [45–47].

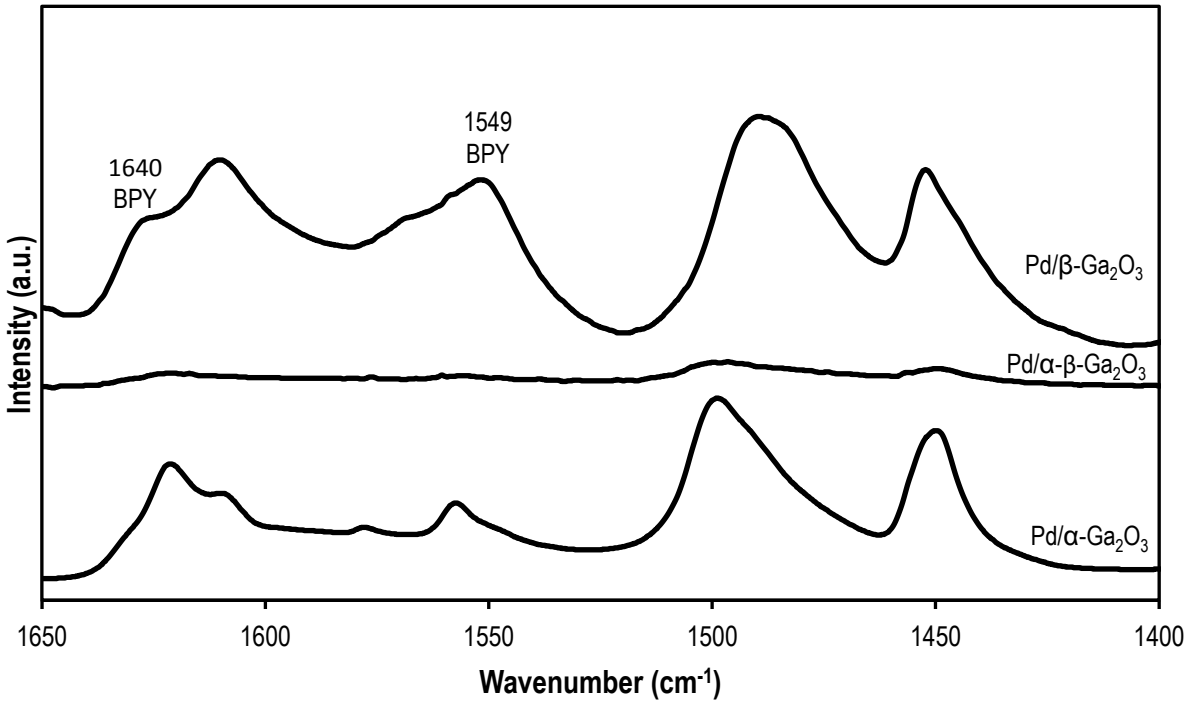


**Figure 14.** Pyridine adsorption FTIR spectra for Pd on $Ga_2O_3$ polymorphs al 473 K.

### 3.6 SEM

The SEM micrographs for different $Ga_2O_3$ phases are shown in Figure 15. In these micrograms we can see that there is no difference in the particle morphology of the samples we synthesized, all the phases appear agglomerated with individual crystallites with ellipsoidal structure. The LS-$Ga_2O_3$ has a different morphological structure, the particles have a cubic shape. These micrographs show that there is no effect of thermal treatments on the morphology of the particles.

Figure 16 shows the SEM micrograms for silica supports, $SiO_2$ and SBA-15. In these micrographs we can see the completely amorphous shape of the $SiO_2$ particles compared with a SBA-15 fiber-like morphology.

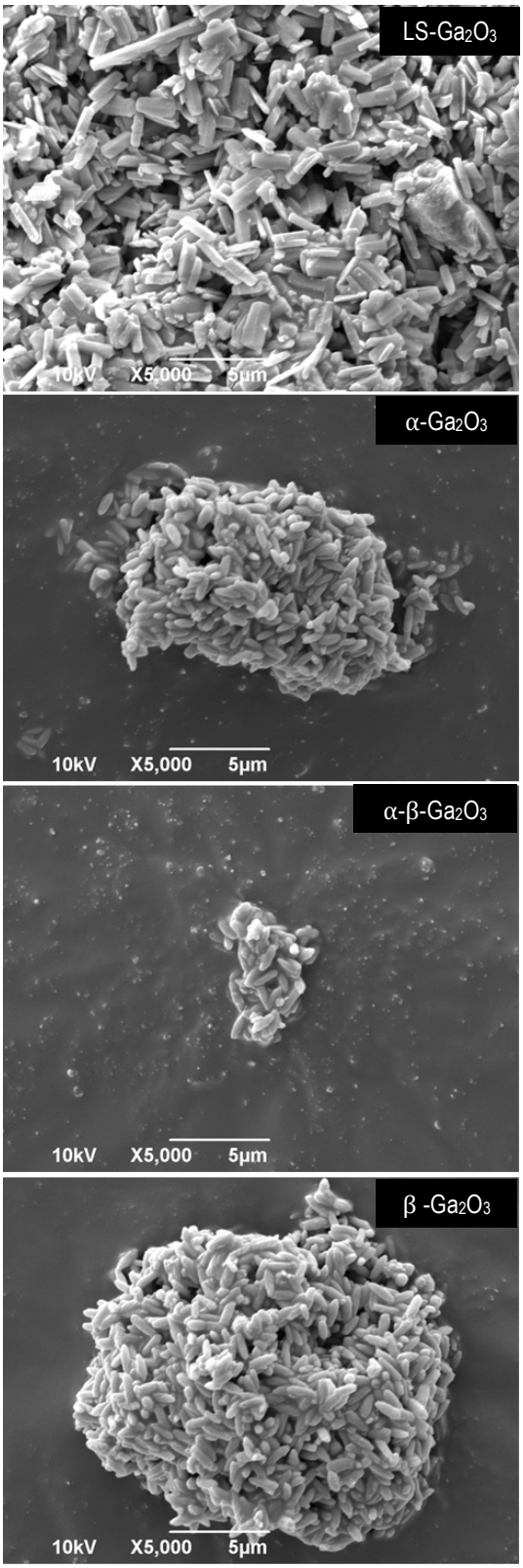


**Figure 15.** SEM micrographs for $Ga_2O_3$ crystalline phases.

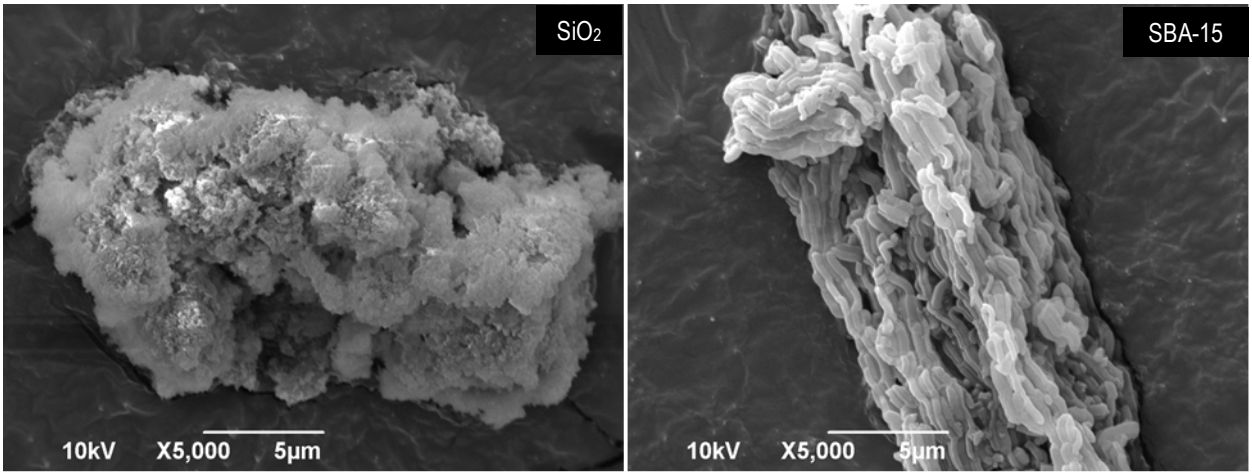


**Figure 16.** SEM micrograms for Silica catalysts supports.

# Chapter 4

## 4. Catalytic Performance

### 4.1 Cu-ZnO, Cu-ZnO-$Ga_2O_3$ and Pd-$Ga_2O_3$ supported on silica

Initially the main objective was to make a screening of potential catalysts for the hydrogenation of $CO_2$. The three main candidates were Cu-ZnO, Cu-ZnO-$Ga_2O_3$ and Pd-$Ga_2O_3$. These three catalysts supported on commercial $SiO_2$ were evaluated based on the conversion obtained. This set of reactions were carried out at 543 K and 0.69 MPa with 27 ml/min $CO_2$ and 123 ml/min $H_2$. Table 4 shows the conversion at steady state obtained for Cu-ZnO, Cu-ZnO-$Ga_2O_3$ and Pd-$Ga_2O_3$ catalysts supported on $SiO_2$. At these conditions the difference between the conversions is not significant. The highest conversions were obtained Cu-ZnO-$Ga_2O_3$ and Pd-$Ga_2O_3$ supported catalysts. The difference between Cu-ZnO and Cu-ZnO-$Ga_2O_3$ may be due to an increase in basic sites to adsorb $CO_2$ by the addition of the $Ga_2O_3$, thus allowing the $CO_2$ hydrogenation. On the other hand the difference between Cu-ZnO-$Ga_2O_3$ and Pd-$Ga_2O_3$ catalysts appears to be due to the ability of palladium to hydrogenate [48–50]. It is known that Pd is a metal with a greater capacity for hydrogenate than Cu [8,51].

**Table 4.** Surface properties and reaction results for catalysts supported on silica

| Catalyst | Lewis Sites (mmol/g) | Brønsted Sites (mmol/g) | Metal Sites (mmol/g) | $X_{CO2}$ (%) | TOF ($s^{-1}$) | $CH_3OH$ Selectivity (%) |
|---|---|---|---|---|---|---|
| Cu-ZnO/$SiO_2$(*) | - | - | - | 1.2 | - | 100 |
| Cu-ZnO-$Ga_2O_3$/$SiO_2$ | - | - | - | 1.6(*) 2.0 | - | 100(*) 100 |
| Pd-$Ga_2O_3$/$SiO_2$ | 0.0148 | 0.0025 | 0.0003 | 2.2(*) 4.0 | 1(*) 21 | 92(*) 74 |
| Pd-$Ga_2O_3$/SBA-15 | 0.0063 | 0.0008 | 0.0012 | 3.0 | 3 | 35 |

(*)Reaction conditions: 0.69 MPa, 543 K, 27 ml/min $CO_2$ and 123 ml/min $H_2$. The other tabulated values where obtained at 1.72 MPa, 543 K, 10 ml/min $CO_2$, 75 ml/min $H_2$ and 15 ml/min $N_2$.

The reaction conditions were modified to increase the $CO_2$ concentration in order to observe a change in the conversion. The reaction conditions were modified to 543 K and 1.72 MPa with 10 ml/min $CO_2$, 75 ml/min $H_2$ and 15 ml/min $N_2$. At these conditions were studied the catalysts with the highest conversions obtained at the first conditions studied. The only reaction product of $CO_2$ hydrogenation over Cu-ZnO-$Ga_2O_3$ catalyst at these conditions is methanol. Dimethyl ether (DME) is the second product obtained using Pd-$Ga_2O_3$ catalyst. The DME production comes from methanol dehydration over acidic sites of the $Ga_2O_3$ [52–54]. The conversions and selectivities for these materials were calculated at steady state. Table 4 includes the conversions and selectivities obtained for Cu-ZnO-$Ga_2O_3$ and Pd-$Ga_2O_3$ supported on $SiO_2$. The highest conversion were obtained over Pd-$Ga_2O_3$/$SiO_2$ catalyst, consistent with the work of Fujitani and Bonivardi [8,30]. This material exhibits higher conversions of $CO_2$ at different reaction conditions. For that reason it was decided to continue this work using catalysts composed of palladium and gallium mainly.

Since the material containing Pd-$Ga_2O_3$ apparently have better catalytic properties for the hydrogenation of $CO_2$, Pd-$Ga_2O_3$ catalysts supported on $SiO_2$ and SBA-15 were tested at 543 K and 1.72 MPa with 10 ml/min $CO_2$ 75 ml/min $H_2$ and 15 ml/min $N_2$. The main reaction product of $CO_2$ hydrogenation over Pd-$Ga_2O_3$ catalysts at these conditions is methanol. The conversions, selectivities, yields and TOFs for these materials were calculated at steady state. Table 4 shows metal sites compared with the conversion and TOF for Pd-$Ga_2O_3$ catalysts supported on $SiO_2$ and SBA-15. The highest conversion was obtained with Pd-$Ga_2O_3$/$SiO_2$, even though it is the catalyst with the lowest surface area. This catalyst also has the highest TOF with the lowest availability of metal sites. Therefore, we speculate that this behavior may be attributed to the formation of an intermetallic compound between Pd and Ga. The characterization that was done for these materials is not sufficient to prove this hypothesis, to probe that must be performed XPS characterization, which could not be performed due to shortage of sample.

Table 4 shows the selectivity and yield obtained for Pd-$Ga_2O_3$ catalysts supported on $SiO_2$ and SBA-15 related to the number of acid sites. The highest number of acid sites per unit of mass was obtained over Pd-$Ga_2O_3$/$SiO_2$, but this material shows the lowest selectivity to DME. Based on these results we cannot conclude whether there is an effect on the increase in Brønsted or Lewis sites on the selectivity for DME, nor if the ratio of Brønsted/Lewis sites has an effect. Hence, the high selectivity to DME over Pd-$Ga_2O_3$/SBA-15 can be attributed to an effect of structure or surface area [55].

During the reactions a change in selectivity over time on stream was observed. Figure 17 shows the change in methanol and DME selectivity over time on stream for Pd-$Ga_2O_3$ catalysts supported over $SiO_2$ and SBA-15. In both cases the first product observed was DME and then over time methanol was observed. In the case of Pd-$Ga_2O_3$/$SiO_2$, Figure 17 A, the selectivity to

methanol increases over time on stream and becomes higher than the selectivity to DME after 5 hours. At steady state the selectivity to methanol is greater over this material. On the other hand, the selectivity to methanol over Pd-$Ga_2O_3$/SBA-15 increases over time on stream but does not become higher than the selectivity to DME, as shown in Figure 17 B. This behavior was observed for both materials, in which a higher selectivity to DME was observed during the first five hours of reaction. This can be attributed to the low concentration of methanol initially produced. In other words, the reaction rate for DME formation from methanol may be changing by the increment in methanol concentration over time on stream until the steady state is reached.

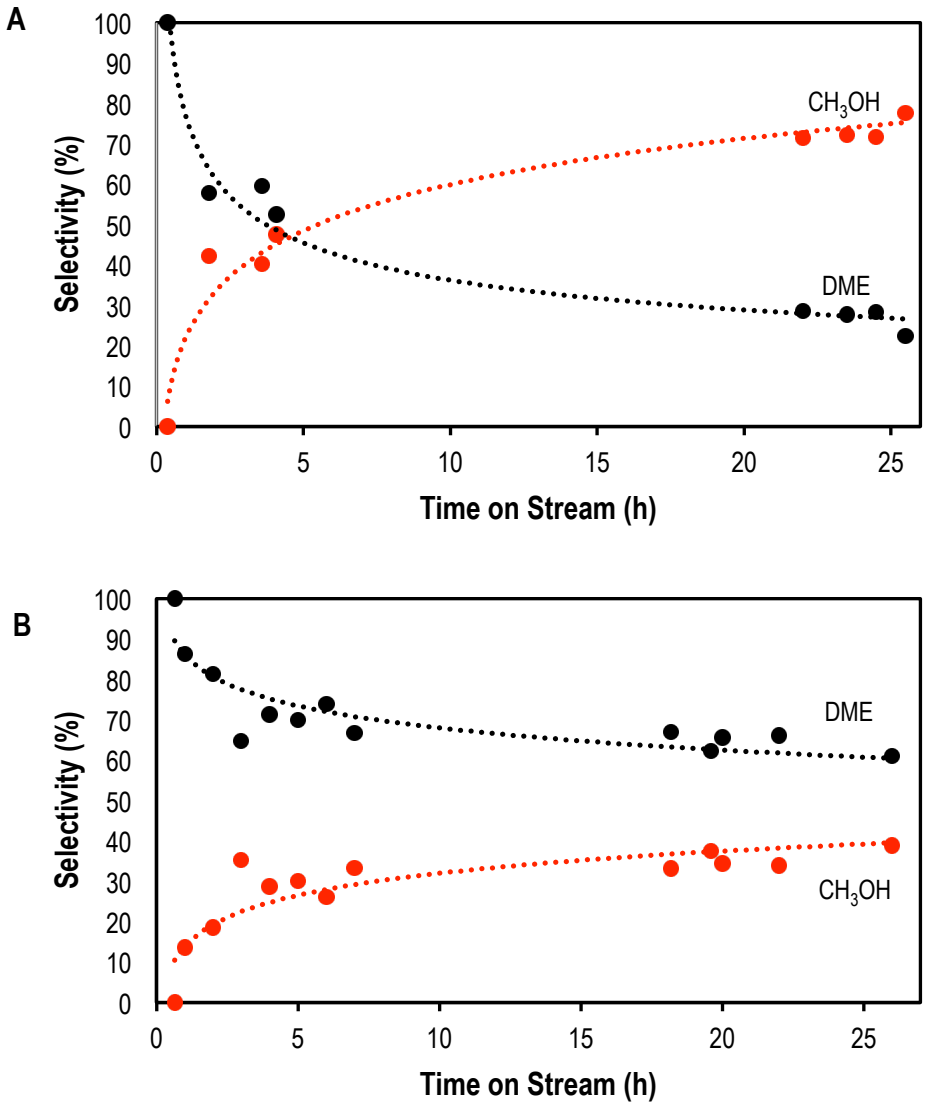


**Figure 17. A** Methanol and DME selectivity over Pd-$Ga_2O_3$/$SiO_2$, **B** Methanol and DME selectivity over Pd-$Ga_2O_3$/SBA-15.

### 4.2 Pd supported on $Ga_2O_3$ polymorphs

Table 5 shows surface properties and reaction results for Pd catalysts supported on $Ga_2O_3$ polymorphs. The TOF changes between $Ga_2O_3$ polymorphs and increases with the increment in the $Pd_2Ga$ content on the catalyst surface. The catalysts with the β-$Ga_2O_3$ crystal phase have the highest TOF. These catalysts supported on β-$Ga_2O_3$ have the highest content of $Pd_2Ga$ on the

surface. The content of the intermetallic compound $Pd_2Ga$ depends on the $Ga_2O_3$ polymorphs, and the increase of the $Pd_2Ga$ content over the surface increases the catalysts activity. Whereby the catalyst activity depends mainly on the $Ga_2O_3$ crystalline structure and the quantity of $Pd_2Ga$ on the surface.

**Table 5.** Pd supported on $Ga_2O_3$ polymorphs properties and reaction results

| **Catalyst** | **Lewis Sites (mmol/g)** | **Brønsted Sites (mmol/g)** | **Metal Sites (mmol/g)** | **Pd Content (%)** | **$Pd_2Ga$ Content (%)** | **$\Delta H_{CO2}^{ads}$ (kJ/mol)** | **$X_{CO2}$ (%)** | **TOF ($s^{-1}$)** |
|---|---|---|---|---|---|---|---|---|
| Pd/α-$Ga_2O_3$ | 0.003 | 0.004 | 0.063 | 67.43 | 32.57 | 17.22 | 13 | 0.26 |
| Pd/α-β-$Ga_2O_3$ | 0.001 | 0.001 | 0.067 | 70.97 | 29.03 | 21.60 | 11 | 0.21 |
| Pd/β-$Ga_2O_3$ | 0.009 | 0.021 | 0.002 | 21.71 | 78.29 | 15.30 | 11 | 7.43 |
| Pd/LS-$Ga_2O_3$ | 0.001 | 0.001 | 0.014 | 22.14 | 77.86 | - | 11 | 0.94 |

As mentioned above, the ratio of bicarbonate and bidentate species adsorbed on the surface changes between catalysts and the ratio that best approaches one is on the catalysts supported over β-$Ga_2O_3$ polymorphs. Figure 18 shows the TOF related to the ratio of $CO_2$ adsorption type area. When the ratio is close to one the TOF increases. This behavior suggests that the increase in the catalyst activity for $CO_2$ hydrogenation is also promoted by the formation of the bidentate carbonate species over the surface.

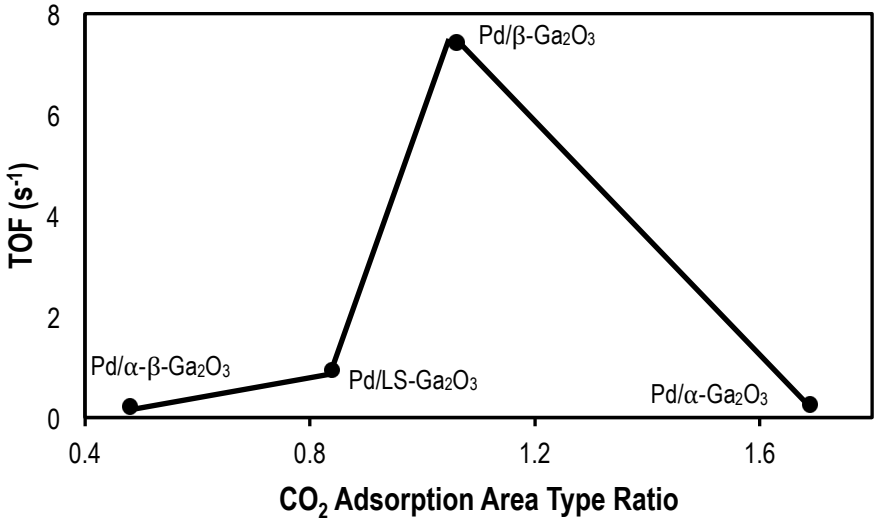


**Figure 18.** Turn over frequency related to the $CO_2$ adsorption type ratio.

An analysis of the change in conversion of $CO_2$ as a function of time on stream (TOS) indicates that there is some deactivation for all samples studied as shown in Figure 19. Pd/α-β-$Ga_2O_3$ is the catalyst that has the highest deactivation with TOS. This catalyst has the lowest $Pd_2Ga$ content, this suggests that the α-β-$Ga_2O_3$ is the less stable polymorphs at the experimental conditions used here. The decrease in $CO_2$ conversion can be attributed to the catalyst deactivation caused by a reduction of the number of basic active sites on the $Ga_2O_3$ polymorphs [56]. The reduction of basic sites over $Ga_2O_3$ was confirmed by comparing the $CO_2$ adsorption isotherms of Pd/α-β-$Ga_2O_3$ before and after reaction, as shown in Figure 20. The $CO_2$ uptake over Pd/α-β-$Ga_2O_3$ decreases after reaction. The reduction of $Ga_2O_3$ is induced by the spill of atomic hydrogen activated by Pd inducing the formation of $Pd_2Ga$, as explained in section 3.3 [9,41]. Hence, the reduction of $Ga_2O_3$ can cause a decrease in the number of basic sites on the surface by the loss of oxygen in the structure. Therefore, it could be that catalyst deactivation is

due to the loss of basic sites by the reduction of $Ga_2O_3$ by the exposure to high concentrations of $H_2$ at high temperature during the reaction.

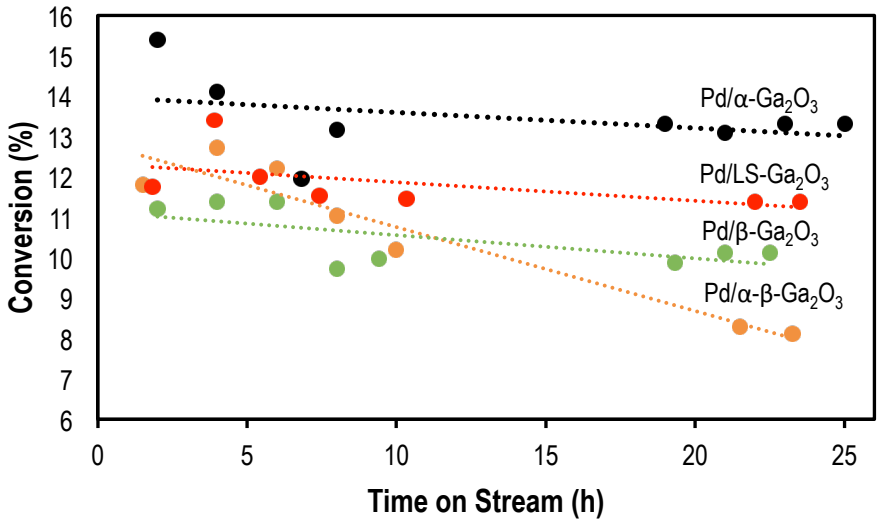


**Figure 19.** $CO_2$ conversion over time on stream for Pd catalysts supported on $Ga_2O_3$ polymorphs.

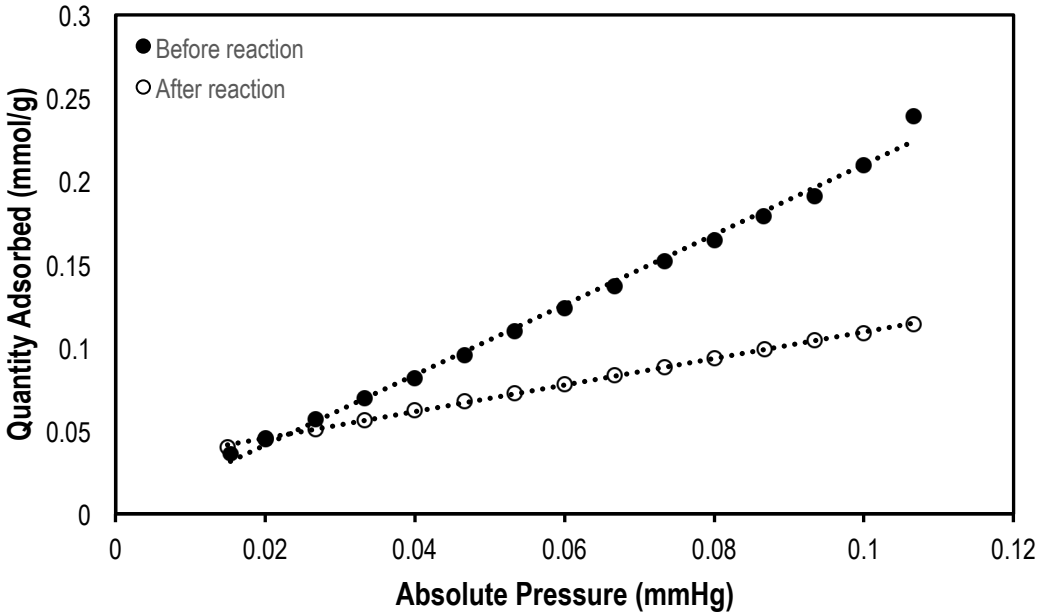


**Figure 20.** $CO_2$ adsorption isotherms over Pd/α-β-$Ga_2O_3$ before and after reaction.

Table 5 shows methanol and DME selectivity and the number of acid sites over Pd supported on $Ga_2O_3$ polymorphs catalysts. The selectivity to DME apparently increases with the increment in acid sites number. The highest selectivity to DME was obtained over Pd/α-$Ga_2O_3$ and Pd/β-$Ga_2O_3$. Several reaction mechanisms for methanol conversion to DME have been proposed; some attributed the responsibility of the dehydration of methanol to DME to the Brønsted sites, other attribute it to the Lewis sites [57–61]. Based on the results obtained in this study, is not observed if there is a preference for Brønsted or Lewis sites. Therefore, the dehydration of methanol to DME over Pd catalysts supported on $Ga_2O_3$ polymorphs may be favored by both type of acidity. Hence, the difference in selectivity to dimethyl ether may be due only to the increase in the number of acidic sites. This behavior was also observed by Ramos and co-workers in the dehydration of methanol to DME over $Al_2O_3$, $ZrO_2$ and ZSM-5 [62]. Figure 21 shows the Brønsted/Lewis ratio for Pd supported catalysts over $Ga_2O_3$ polymorphs. These results show a maximum in 1.45. Therefore, the selectivity to DME may be also influenced by the ratio of the acid types.

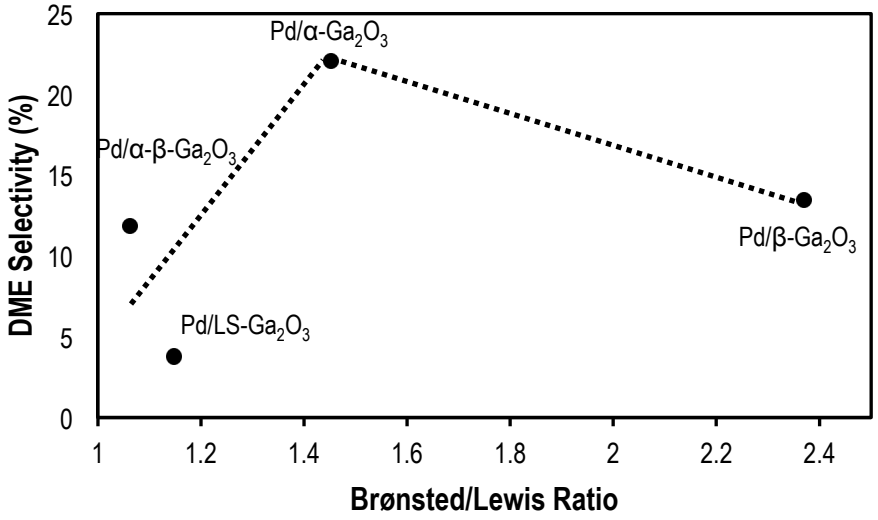


**Figure 21.** DME selectivity in relation to Brønsted/Lewis ratio.

### 4.4 Kinetic Study

A kinetic study was conducted using Pd/LS-$Ga_2O_3$ catalyst to determine the order of reaction with respect to $CO_2$. The initial reaction rates ($-r_i$) were calculated for three $CO_2$ concentrations; $1.91x10^{-5}$, $3.82x10^{-5}$ and $4.58x10^{-5}$ mol/ml at 543 K and 1.72 MPa. The rates obtained for each concentration were determined by plotting the conversion at different catalysts mass/$CO_2$ mass flow ratios, as shown in Figure 22. The slope of this curve is equal to the speed of initial reaction at that concentration. To calculate the reaction order the logarithm of the initial reaction rates is plotted in relation to the logarithm of the initial $CO_2$ concentration, as shown in Figure 23. The slope of this curve is equal to the reaction order related to $CO_2$. The reaction order obtained for $CO_2$ hydrogenation over Pd/LS-$Ga_2O_3$ is -0.2, which state that to high concentrations of $CO_2$ the reaction occurs more slowly.

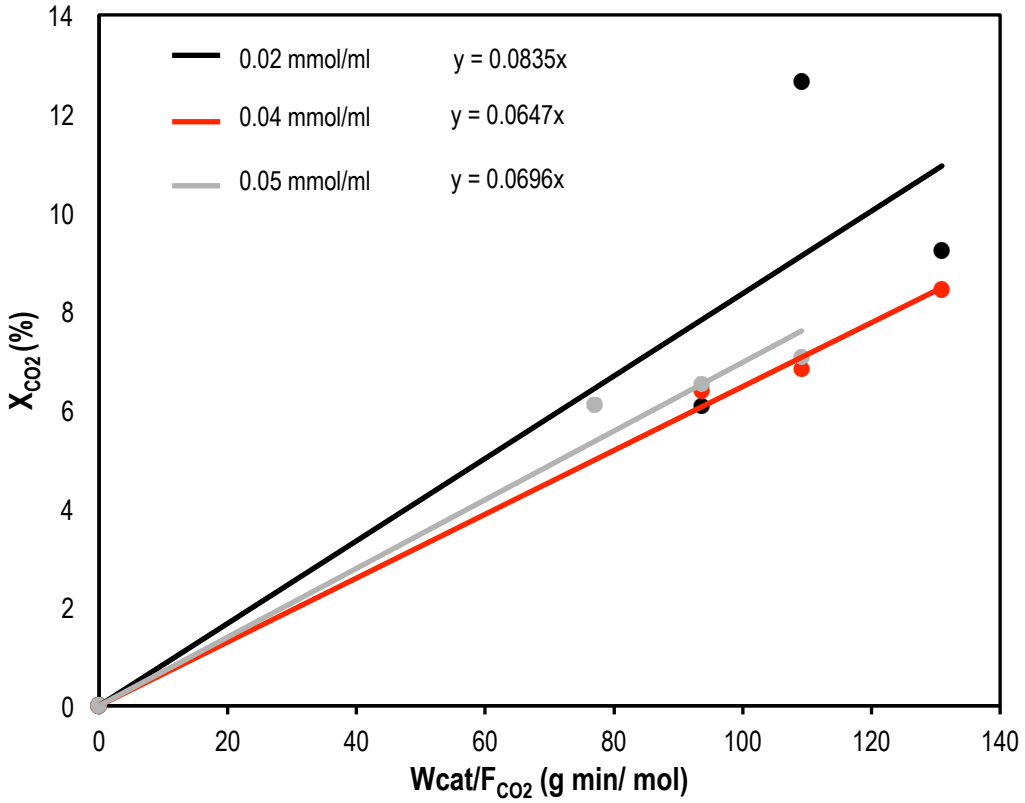


**Figure 22.** $CO_2$ conversion related to the ratio of catalyst mass and $CO_2$ molar flow.

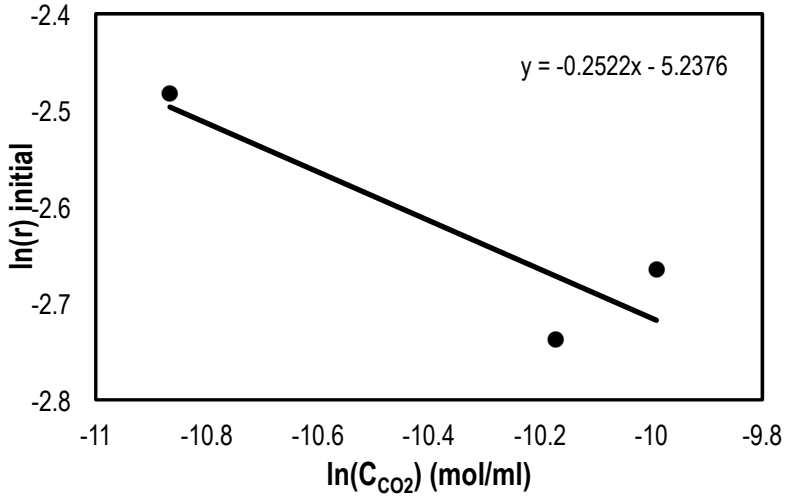


**Figure 23.** Initial reaction rate logarithms related to the $CO_2$ initial concentration logarithms.

# Chapter 5

## 5. The effect of Niobium species in $CO_2$ conversion

### 5.1 Increased selectivity to DME by the addition of $Nb_2O_5$ on Pd/LS-$Ga_2O_3$

As mentioned above, the DME comes from the dehydration of methanol as a result of the acidity of $Ga_2O_3$. Based on this, niobium oxide ($Nb_2O_5$) was added to Pd/LS-$Ga_2O_3$ surface in an attempt to increase the selectivity to DME. $Nb_2O_5$ is often used in dehydration reactions due to its high acidity [63–66].

The catalyst was prepared by the deposition of Pd nitrate and Nb chloride precursors over LS-$Ga_2O_3$ surface by evaporative deposition. The Pd precursor was first deposited over the surface, then the material was dried at 313 K. After 24 hours of drying the Nb precursor was deposited, then the material was dried at 313 K. After the deposition of both precursors the material was calcined at 673 K in an air atmosphere, followed by reduction at 573 K. The resulting material is Pd-$Nb_2O_5$/LS-$Ga_2O_3$ with 2.7 wt % Pd and 1.4 wt % Nb. The surface area obtained for this catalyst was 19 $m^2$/g. The reactions were carried out at 543 K, 1.72 MPa, 10 ml/min $CO_2$, 75 ml/min $H_2$ and 15 ml/min $N_2$.

Table 6 shows the TOF, conversion and selectivity obtained for Pd-$Nb_2O_5$/LS-$Ga_2O_3$ compared with Pd/LS-$Ga_2O_3$. The conversion obtained over Pd-$Nb_2O_5$/LS-$Ga_2O_3$ is less than that obtained with Pd/LS-$Ga_2O_3$. On the other hand, the TOF and DME selectivity obtained for Pd-$Nb_2O_5$/LS-$Ga_2O_3$ are higher than that obtained with Pd/LS-$Ga_2O_3$.The addition of $Nb_2O_5$ on the

surface increases the selectivity to DME of a 0% to 54%. Thus, this demonstrates that the selectivity to DME can be enhanced by the addition of an acidic species on the catalyst surface.

In this experiment no reaction products were observed until after one hour on stream. Figure 24 shows the change in methanol and DME over time on stream. The first product that was observed was DME and was the only product observed for 8 hours on stream. After 9 hours the production of methanol was observed. The DME selectivity decreased from 100% to 53 % between the 10 and 20 hours on stream, after 20 hours on stream is relatively constant. These results show that the selectivity to DME can be enhanced by the addition of $Nb_2O_5$ on the surface and that increase remains constant once the steady state is reached.

**Table 6.** Comparison between Pd/LS-$Ga_2O_3$ and Pd-$Nb_2O_5$/LS-$Ga_2O_3$ selectivity and conversion at steady state

| **Catalyst** | **Surface Area ($m^2/g$)** | **TOF ($s^{-1}$)** | **$X_{CO2}$ (%)** | **DME Selectivity (%)** |
|---|---|---|---|---|
| Pd/LS-$Ga_2O_3$ | 27 | 0.9 | 6 | 0 |
| Pd-$Nb_2O_5$/LS-$Ga_2O_3$ | 19 | 1.5 | 5 | 53 |

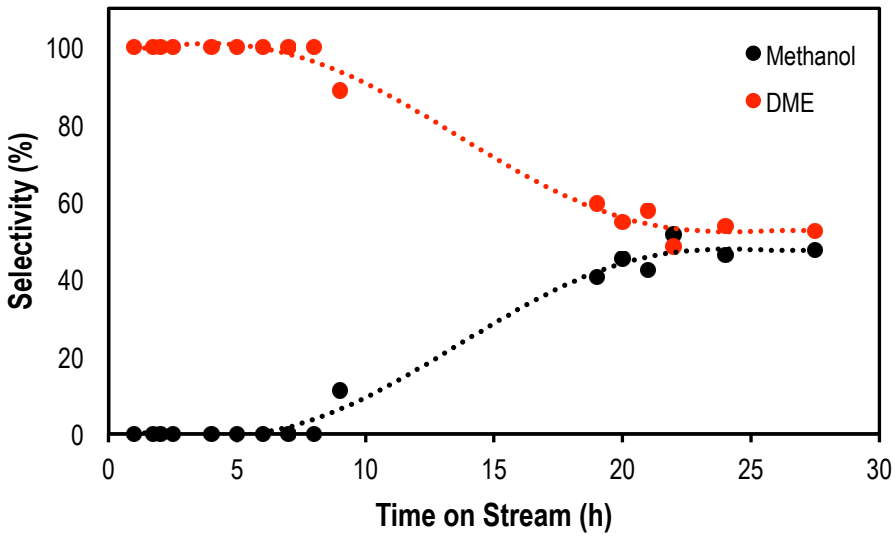


**Figure 24.** Methanol and DME selectivity over Pd-$Nb_2O_5$/LS-$Ga_2O_3$.

### 5.2 $CO_2$ hydrogenation over Pd supported on $Nb_2O_5$ and $NbOPO_4$ catalysts

The $Nb_2O_5$ and $NbOPO_4$ were obtained from Companhia Brasileira De Metalurgia e Mineração (CBMM). The catalysts were prepared by the deposition of Pd nitrate precursor over $Nb_2O_5$ and $NbOPO_4$ surface by evaporative deposition. The Pd precursor was deposited over the surface, then the material was dried at 313 K, calcined at 673 K in an air atmosphere and reduced at 573 K. The resulting materials are Pd/$Nb_2O_5$ and Pd/$NbOPO_4$ with 2 wt % Pd. The surface area obtained for Pd/$Nb_2O_5$ and Pd/$NbOPO_4$ were 89 $m^2/g$ and154 $m^2/g$, respectively. The reactions were carried out at 543 K, 1.72 MPa, 10 ml/min $CO_2$ and 90 ml/min $H_2$. Nitrogen was not used as internal standard because the products signals on the chromatogram, in this case, coincides with that of $N_2$.

Figure 25 shows the XRD patterns for Pd/$Nb_2O_5$ and Pd/$NbOPO_4$. As seen in the figure, the niobium oxide has a diffraction pattern that corresponds to a crystalline structure; whereas the niobium phosphate appears amorphous, whereby the material has an amorphous structure. In

the diffraction pattern for $Pd/NbOPO_4$ we can observe the characteristic peaks of metallic palladium at $40^o$ and $47^o$. On the other hand, in the diffractogram for $Pd/Nb_2O_5$ palladium peaks are overlapped with peaks that correspond to $Nb_2O_5$ at $47^o$ and an intermetallic compound between Pd and Nb at $40^o$. The identified intermetallic compound is $Pd_3Nb$ [67]. Other peaks observed match in number and relative intensities to the peaks for monoclinic $Nb_2O_5$ (JCPDS Card No. 37-1468), but are shifted $6.5^o$ to the right. Several $Nb_2O_5$ polymorphs were identified at different synthesis conditions: T-$Nb_2O_5$, B-$Nb_2O_5$, H-$Nb_2O_5$, M-$Nb_2O_5$, N-$Nb_2O_5$, P-$Nb_2O_5$, R-$Nb_2O_5$ and TT-$Nb_2O_5$ [68–74]. The polymorph identified in $Pd/Nb_2O_5$ corresponds to H-$Nb_2O_5$. Nico and co-workers, demonstrated that the formation of the different $Nb_2O_5$ polymorphs depends on the calcination temperature [75]. Therefore, the shift in the peaks of $Nb_2O_5$ may be caused to a change in crystalline phase by the exposure to air at 673 K.

Table 7 shows the conversions and selectivities at steady state obtained for $Pd/Nb_2O_5$ and $Pd/NbOPO_4$. The conversion obtained at these reaction conditions are the same for both catalysts. The only product formed when $Pd/NbOPO_4$ is used was carbon monoxide. The conversion of $CO_2$ and $H_2$ to CO and $H_2O$ is known as reverse water gas shift reaction (RWGS) [76,77]. Carbon monoxide and a small quantity of $CH_4$ were formed on $Pd/Nb_2O_5$. The selectivity for $CH_4$ at steady state was only 3 %. Methane production comes from the hydrogenation of CO by Pd [78,79]. The formation of $CH_4$ depends on the support and the interaction that has with the Pd [78,79]. Figure 26 shows the $CO_2$ adsorption isotherms for $Pd/Nb_2O_5$ and $Pd/NbOPO_4$. Both samples adsorbs $CO_2$ suggesting the presence of basic sites for $CO_2$ adsorption. These adsorption and reaction results suggest that the Nb supports have basic active sites that allow the $CO_2$ conversion to other products.

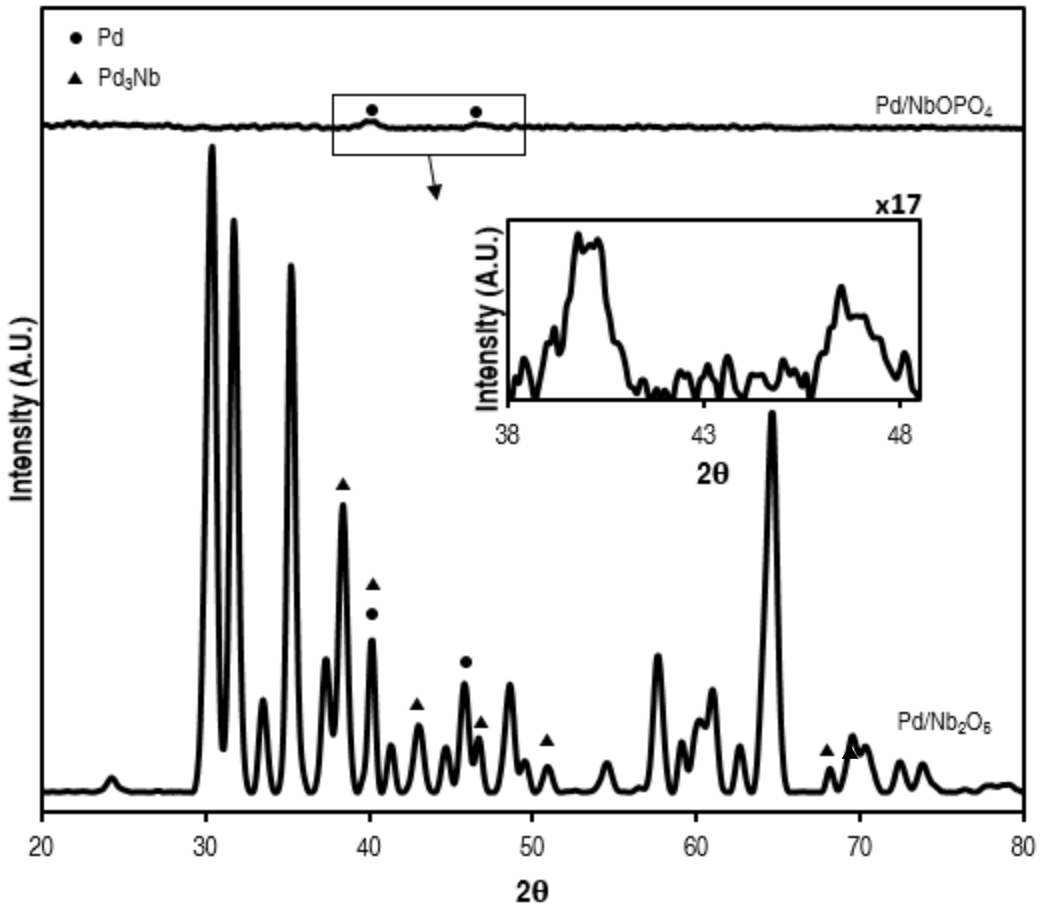


**Figure 25.** XRD patterns for $Pd/Nb_2O_5$ and $Pd/NbOPO_4$.

**Table 7.** Steady state conversion and selectivities obtained over $Pd/Nb_2O_5$ and $Pd/NbOPO_4$

| **Catalyst** | **Surface Area ($m^2/g$)** | **Metal sites (mmol/g)** | **$X_{CO2}$ (%)** | **CO Selectivity (%)** | **$CH_4$ Selectivity (%)** | **TOF ($s^{-1}$)** |
|---|---|---|---|---|---|---|
| $Pd/Nb_2O_5$ | 89 | 0.07 | 9 | 97 | 3 | 0.18 |
| $Pd/NbOPO_4$ | 154 | 0.14 | 9 | 100 | 0 | 0.08 |

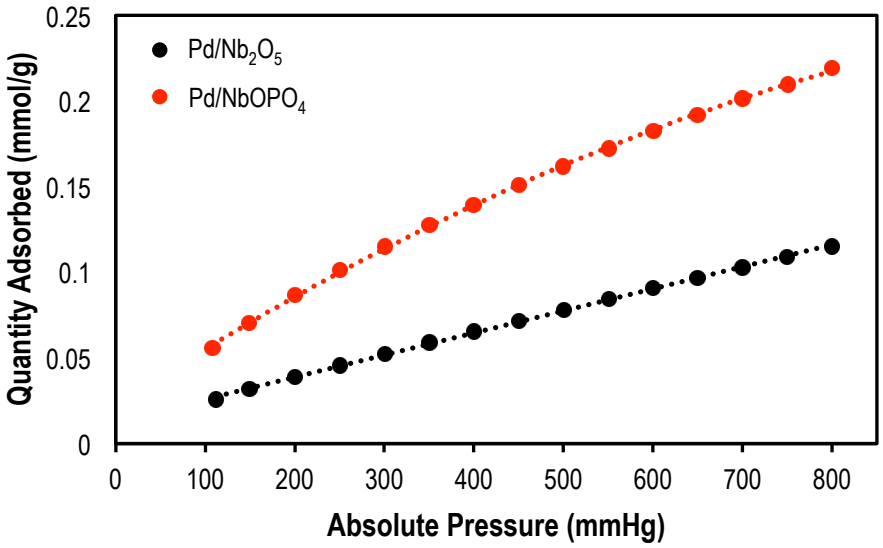


**Figure 26.** $CO_2$ adsorption isotherms at 308 K for $Pd/Nb_2O_5$ and $Pd/NbOPO_4$

# *Chapter 6*

## 6. Synthesis of mesoporous $Ga_2O_3$

### 6.1 Synthesis procedure and results

Materials with a defined pore structure and pore size of mesoporous range are characterized by a high surface area. The increase in surface area leads to an increase in the number of places available for the adsorption of molecules. In the case of catalysts, this increase in adsorption leads to an increase in the quantity of adsorbed molecules available to react, therefore an increase in the conversion is possible. Based on these principles it was decided to synthesize a mesoporous $Ga_2O_3$ to be used as catalyst support in future $CO_2$ hydrogenation reactions.

The synthesis of this material was carried out in three main steps: SBA-15 synthesis, CMK-3 synthesis and finally the formation of mesoporous gallium [80]. Figure 27 summarizes the mesoporous $Ga_2O_3$ synthesis process. The SBA-15 is synthesized using Pluronic (P-123) as template and tetraethyl orthosilicate (TEOS) as silica precursor, following the procedure reported by Stucky and co-workers [37]. Calcined SBA-15 was impregnated two times using an acid sucrose base solution, following the procedure reported by Michorczyk and co-workers [81]. For the first impregnation the solution contained 1.25 g of sucrose, 0.14 g $H_2SO_4$ sulfuric acid and 5.0 g deionized water per gram of SBA-15. The mixture was placed in a drying oven for 12 hours at 373 K. The sample turned dark brown or black during the treatment in the oven. The

silica sample, containing partially polymerized and carbonized sucrose at the present step, was treated again at 373 K using the same drying oven after the addition of the second impregnation solution. The second impregnation solution contained 0.8 g of sucrose, 0.09 g $H_2SO_4$ sulfuric acid and 3 g deionized water per gram of SBA-15. The carbonization was completed by pyrolysis at 1173 K with a heating rate of 1 K/min and 50 ml/min He. The carbon-silica composite obtained after pyrolysis was washed twice with a 10 wt % hydrofluoric acid (HF) in deionized water solution at room temperature, to remove the silica template. The template-free carbon product thus obtained was filtered and washed with distilled water. Mesoporous $Ga_2O_3$ was prepared with two impregnation steps from the prepared CMK-3, following the procedure reported by Michorczyk and co-workers [80]. The CMK-3 carbon sieves were first impregnated with 4 ml of a Tetrahydrofuran (THF) solution containing 1 M of Ga ions per CMK-3 gram. Then the sample was dried at 353 K for 2 hours. These last two steps were repeated in the same order. The dried sample was calcined in two steps, first it was heated from room temperature to 523 K with a heating rate of 1 K/min followed by isothermal heating at 543 K for 2 hours. The previous step is done to remove the nitrates from the gallium precursor. To crystallize the gallium on the CMK-3 surface the sample was heated flowing 50 ml/min He from room temperature to 1073 K with a heating rate of 1 K/min followed by isothermal heating at 1073 K for 10 hours. Then the sample was heated from room temperature to 873 K with a heating rate of 1 K/min followed by isothermal heating at 873 K for 10 hours. The last step consists of the removal of the CMK-3 from the $Ga_2O_3$.

Table 8 summarizes the results of the porosity analysis for SBA-15, CMK-3 and mesoporous $Ga_2O_3$. The synthesized SBA-15 and CMK-3 exhibit a high surface area and a pore diameter and a pore size corresponding to those obtained in the literature [37,81]. The surface

area obtained for $Ga_2O_3$ was 24 $m^2/g$, much lower than that obtained by Michorczyk and co-workers [80]. The isotherm obtained for this material corresponds to an amorphous material, not shown here. Based on these results the sample was calcined again at 973 K to remove carbon residues from the pores. The surface area obtained after calcination at 973 K was 9 $m^2/g$. These results may be attributed to the collapse of the structure by thermal treatment. Figure 28 shows the XRD patterns for SBA-15, CMK-3 and $Ga_2O_3$. The peaks in the XRD patterns for SBA-15 and CMK-3 corresponds to the order of the pores in the structure [37,81]. On the other hand, the XRD pattern at low angles for $Ga_2O_3$ shows no peaks characteristics to an ordered arrangement of pores. Therefore, the mesoporous $Ga_2O_3$ was not successfully synthesized. Figure 29 shows the XRD pattern for $Ga_2O_3$. The XRD pattern for $Ga_2O_3$ shows that the synthesized $Ga_2O_3$ exhibit the β phase. For future mesoporous $Ga_2O_3$ synthesis it is recommended to reduce the calcination temperature or time that the CMK-3 is removed from the $Ga_2O_3$.

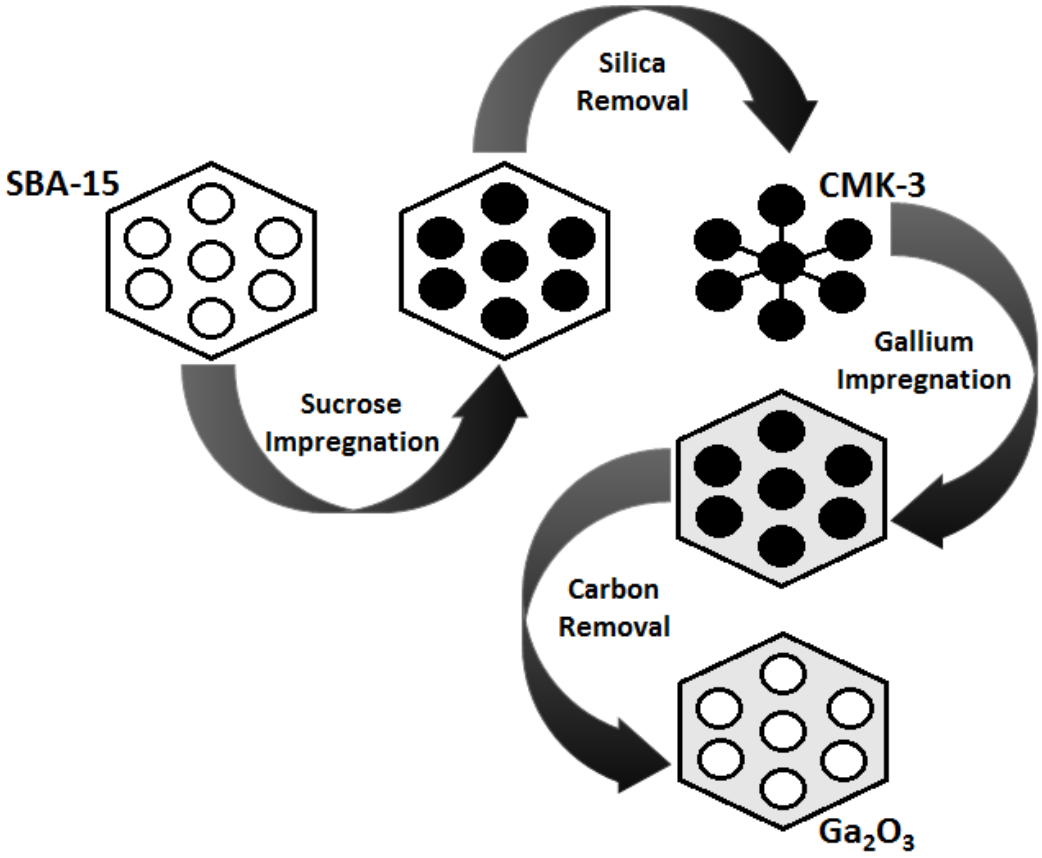


**Figure 27.** Mesoporous $Ga_2O_3$ synthesis.

**Table 8.** Porosity analysis results for mesoporous supports

| Material | Surface Area ($m^2/g$) | Pore Width (nm) | Pore Volume ($cm^3/g$) |
|---|---|---|---|
| SBA-15 | 755 | 8.06 | 1.06 |
| CMK-3 | 1403 | 4.73 | 1.61 |
| $Ga_2O_3$ | $24^{(*)}$ $9^{(\#)}$ | - | - |

$^{(*)}$ Calcined at 873 K, $^{(\#)}$ Calcined at 973 K

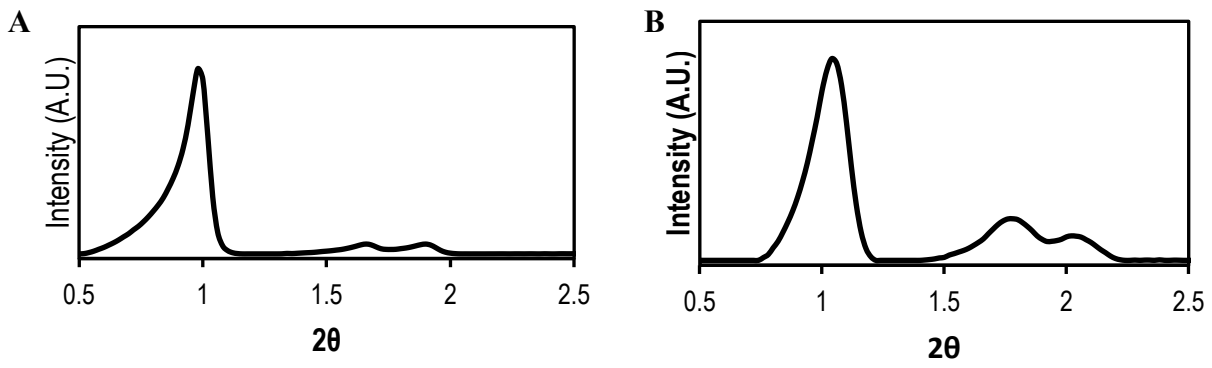


**Figure 28.** XRD patterns for **A** SBA-15 and **B** CMK-3.

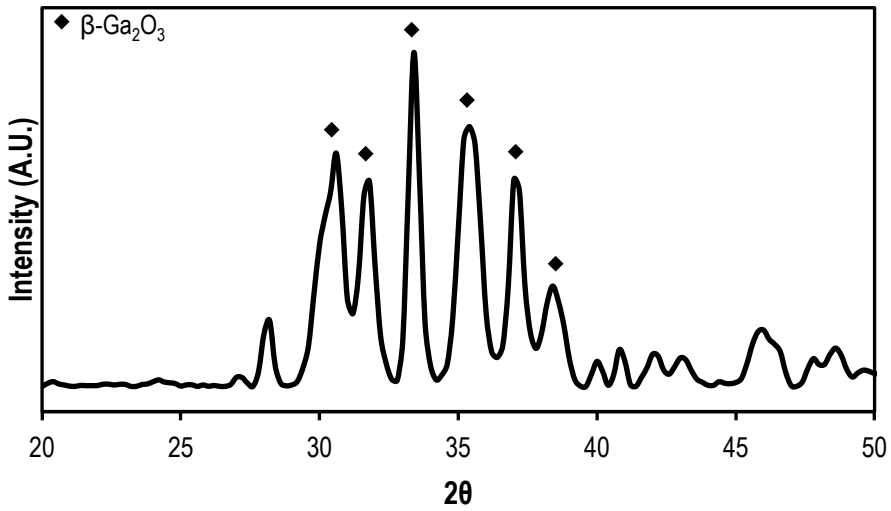


**Figure 29.** XRD pattern for $Ga_2O_3$.

# *Chapter 7*

## 7. Final Remarks: General Conclusions and Contributions

The results presented in this work have confirmed that the Pd-$Ga_2O_3$ catalysts have better catalytic performance than Cu-ZnO catalysts in $CO_2$ hydrogenation. The Pd-$Ga_2O_3$ catalyst supported on $SiO_2$ exhibit a higher conversion than the Cu-ZnO supported on $SiO_2$. Two reactions products are observed using Pd-$Ga_2O_3$ catalysts, methanol and DME. The Pd-$Ga_2O_3$ catalyst supported on $SiO_2$ has a higher $CO_2$ conversion and TOF compared to Pd-$Ga_2O_3$/SBA-15, but the selectivity to DME is two times higher using the catalyst supported on SBA-15.

This work also showed some insights in understanding the effect of the $Ga_2O_3$ polymorphism and the formation of the intermetallic compound $Pd_2Ga$ in $CO_2$ hydrogenation to methanol and DME. The catalytic activity of Pd supported over $Ga_2O_3$ is enhanced by the formation and the increment of the intermetallic compound $Pd_2Ga$. The $Pd_2Ga$ content varies depending in the $Ga_2O_3$ polymorphs, the formation of this compound is favored over β-$Ga_2O_3$ polymorph. The catalytic activity is also enhanced by the $CO_2$ adsorption properties of $Ga_2O_3$ polymorphs, specifically by the formation of the bidentate carbonate. Palladium catalysts supported on $Ga_2O_3$ show a slight deactivation with time on stream. This deactivation is caused by the reduction of basic sites over $Ga_2O_3$ during the reaction. The catalysts selectivity over Pd supported on $Ga_2O_3$ polymorphs depends on the catalyst acidity, the increment in the number of acid sites increases the conversion of methanol to DME. It's not observed that the selectivity

depends on a specific type of acidity. The formation of the intermetallic compound $Pd_2Ga$ and the type of $Ga_2O_3$ polymorph have a strong impact on the catalytic hydrogenation of $CO_2$.

A kinetic study was carried out in this work using Pd/LS-$Ga_2O_3$. The reaction order obtained was -1, therefore it can be conclude that at high concentrations of $CO_2$ the reaction is slower.

The addition of $Nb_2O_5$ to Pd/LS-$Ga_2O_3$ was also evaluated for the increase in selectivity towards DME. The results presented in this work have confirmed that the addition of $Nb_2O_5$ over the surface increases the selectivity to DME. The selectivity to DME increased from 0 % to 53 %.

This work also showed some results of the $CO_2$ conversion to CO via reverse water gas shift reaction using Pd supported on $Nb_2O_5$ and $NbOPO_4$ catalysts. Both materials show the same conversion percent, but the catalyst supported on niobium oxide shows a low methane production from CO hydrogenation. The results shows that the niobium supports have basic active sites in which $CO_2$ and CO can be converted to other products.

In this work the synthesis of mesoporous $Ga_2O_3$ by nanocasting is also shown. The resulting material has a low surface area and don't have a mesoporous structure. The calcination temperature and time may be influences the formation of the mesoporous $Ga_2O_3$ structure.

# Cited Literature


[1] I. Chorkendorff, Concepts of modern catalysis and kinetics, Wiley-VCH, Weinheim [Germany], 2003.

[2] H.S. Fogler, Elements of chemical reaction engineering, 4th ed, Prentice Hall PTR, Upper Saddle River, NJ, 2006.

[3] T. Ando, 1.2 Inorganic Solid Supported Reagents as Acids and Bases, in: Stud. Surf. Sci. Catal., Elsevier, 1994: pp. 9–20.

[4] M. Tamura, K. Shimizu, A. Satsuma, Comprehensive IR study on acid/base properties of metal oxides, Appl. Catal. Gen. 433-434 (2012) 135–145.

[5] Nanoparticles and catalysis, Wiley-VCH, Weinheim, 2008.

[6] http://www.epa.gov/climatechange/ghgemissions/gases/co2.html, Carbon Dioxide Emissions, EPA, 2013.

[7] J. Toyir, P.R. de la Piscina, J.L.G. Fierro, N. Homs, Highly effective conversion of $CO_2$ to methanol over supported and promoted copper-based catalysts: influence of support and promoter, Appl. Catal. B Environ. 29 (2001) 207–215.

[8] T. Fujitani, M. Saito, Y. Kanai, T. Watanabe, J. Nakamura, T. Uchijima, Development of an active $Ga_2O_3$ supported palladium catalyst for the synthesis of methanol from carbon dioxide and hydrogen, Appl. Catal. Gen. 125 (1995) L199–L202.

[9] L. Li, B. Zhang, E. Kunkes, K. Föttinger, M. Armbrüster, D.S. Su, et al., Ga-Pd/$Ga_2O_3$ Catalysts: The Role of Gallia Polymorphs, Intermetallic Compounds, and Pretreatment Conditions on Selectivity and Stability in Different Reactions, ChemCatChem. 4 (2012) 1764–1775.

[10] K. Fink, Ab initio cluster calculations on the electronic structure of oxygen vacancies at the polar ZnO(000$\bar{1}$) surface and on the adsorption of $H_2$, CO, and $CO_2$ at these sites, Phys. Chem. Chem. Phys. 8 (2006) 1482.

[11] W. Dong, J. Hafner, $H_2$ dissociative adsorption on Pd(111), Phys. Rev. B. 56 (1997) 15396–15403.

[12] S. Wilke, M. Scheffler, Potential-energy surface for $H_2$ dissociation over Pd(100), Phys. Rev. B. 53 (1996) 4926–4932.

[13] Y. Pan, P. Kuai, Y. Liu, Q. Ge, C. Liu, Promotion effects of $Ga_2O_3$ on $CO_2$ adsorption and conversion over a SiO2-supported Ni catalyst, Energy Environ. Sci. 3 (2010) 1322.

[14] G. Mills, H. Jónsson, G.K. Schenter, Reversible work transition state theory: application to dissociative adsorption of hydrogen, Surf. Sci. 324 (1995) 305–337.

[15] N. Iwasa, T. Mayanagi, N. Ogawa, K. Sakata, N. Takezawa, New catalytic functions of Pd–Zn, Pd–Ga, Pd–In, Pt–Zn, Pt–Ga and Pt–In alloys in the conversions of methanol, Catal. Lett. 54 (1998) 119–123.

[16] N. Iwasa, N. Takezawa, New Supported Pd and Pt Alloy Catalysts for Steam Reforming and Dehydrogenation of Methanol, TOP CATAL. 22 (2003) 215–224.

[17] N. Iwasa, W. Nomura, T. Mayanagi, S. Fujita, M. Arai, N. Takezawa, Hydrogen Production by Steam Reforming of Methanol, J. Chem. Eng. Jpn. 37 (2004) 286–293.

[18] N. Iwasa, O. Yamamoto, R. Tamura, M. Nishikubo, N. Takezawa, Difference in the reactivity of acetaldehyde intermediates in the dehydrogenation of ethanol over supported Pd catalysts, Catal. Lett. 62 (1999) 179–184.

[19] N. Iwasa, H. Suzuki, M. Terashita, M. Arai, N. Takezawa, Methanol Synthesis from $CO_2$ Under Atmospheric Pressure over Supported Pd Catalysts, Catal. Lett. 96 (2004) 75–78.
[20] S.E. Collins, D.L. Chiavassa, A.L. Bonivardi, M.A. Baltanás, Hydrogen Spillover in $Ga_2O_3$–$Pd/SiO_2$ Catalysts for Methanol Synthesis from $CO_2/H_2$, Catal. Lett. 103 (2005) 83–88.
[21] T. Fujitani, I. Nakamura, Methanol Synthesis from CO and $CO_2$ Hydrogenations over Supported Palladium Catalysts, Bull. Chem. Soc. Jpn. 75 (2002) 1393–1398.
[22] R. Roy, V.G. Hill, E.F. Osborn, Polymorphism of $Ga_2O_3$ and the System $Ga_2O_3$ —$H_2O$, J. Am. Chem. Soc. 74 (1952) 719–722.
[23] J. Åhman, G. Svensson, J. Albertsson, A Reinvestigation of β-Gallium Oxide, Acta Crystallogr. C. 52 (1996) 1336–1338.
[24] S. Geller, Crystal Structure of β-$Ga_2O_3$, J. Chem. Phys. 33 (1960) 676.
[25] M. Marezio, Bond Lengths in the α-$Ga_2O_3$ Structure and the High-Pressure Phase of Ga2−xFexO3, J. Chem. Phys. 46 (1967) 1862.
[26] A. Haghofer, K. Föttinger, F. Girgsdies, D. Teschner, A. Knop-Gericke, R. Schlögl, et al., In situ study of the formation and stability of supported $Pd_2Ga$ methanol steam reforming catalysts, J. Catal. 286 (2012) 13–21.
[27] M.. Bhargava, A.. Gadalla, K. Schubert, Koexistente phasen vom FeSi-Typ in den mischungen Ni-Pd-Ga und Ni-Pt-Ga, J. Common Met. 42 (1975) 69–76.
[28] K. Khalaff, K. Schubert, Kristallstruktur von $Pd_5Ga_2$, J. Common Met. 37 (1974) 129–140.
[29] S. Penner, H. Lorenz, W. Jochum, M. Stöger-Pollach, D. Wang, C. Rameshan, et al., $Pd/Ga_2O_3$ methanol steam reforming catalysts: Part I. Morphology, composition and structural aspects, Appl. Catal. Gen. 358 (2009) 193–202.
[30] A.L. Bonivardi, D.L. Chiavassa, C.A. Querini, M.A. Baltanás, Enhancement of the catalytic performance to methanol synthesis from $CO_2/H_2$ by gallium addition to palladium/silica catalysts, in: Stud. Surf. Sci. Catal., Elsevier, 2000: pp. 3747–3752.
[31] I.A. Fisher, A.T. Bell, In Situ Infrared Study of Methanol Synthesis from $H_2$/CO over $Cu/SiO_2$ and $Cu/ZrO_2/SiO_2$, J. Catal. 178 (1998) 153–173.
[32] T.C. Schilke, I.A. Fisher, A.T. Bell, In SituInfrared Study of Methanol Synthesis from $CO_2/H_2$ on Titania and Zirconia Promoted $Cu/SiO_2$, J. Catal. 184 (1999) 144–156.
[33] I. Fisher, In-SituInfrared Study of Methanol Synthesis from $H_2/CO_2$ over $Cu/SiO_2$ and $Cu/ZrO_2/SiO_2$, J. Catal. 172 (1997) 222–237.
[34] K. Jung, Role of Hydrogen Spillover in Methanol Synthesis over $Cu/ZrO_2$, J. Catal. 193 (2000) 207–223.
[35] F.-W. Chang, W.-Y. Kuo, K.-C. Lee, Dehydrogenation of ethanol over copper catalysts on rice husk ash prepared by incipient wetness impregnation, Appl. Catal. Gen. 246 (2003) 253–264.
[36] D. Reyes-Luyanda, J. Flores-Cruz, P.J. Morales-Pérez, L.G. Encarnación-Gómez, F. Shi, P.M. Voyles, et al., Bifunctional Materials for the Catalytic Conversion of Cellulose into Soluble Renewable Biorefinery Feedstocks, Top. Catal. 55 (2012) 148–161.
[37] D. Margolese, J.A. Malero, S.C. Christiansen, B.F. Chmelka, G.D. Stucky, Direct Syntheses of Ordered SBA-15 Mesoporous Silica Containing Sulfonic Acid Groups, Chem. Mater. 12 (2000) 2448–2459.

[38] X. Wang, Q. Xu, M. Li, S. Shen, X. Wang, Y. Wang, et al., Photocatalytic Overall Water Splitting Promoted by an α-β phase Junction on $Ga_2O_3$, Angew. Chem. Int. Ed. 51 (2012) 13089–13092.
[39] H. Lorenz, R. Thalinger, E.-M. Köck, M. Kogler, L. Mayr, D. Schmidmair, et al., Methanol steam reforming: $CO_2$-selective $Pd_2Ga$ phases supported on α- and γ-$Ga_2O_3$, Appl. Catal. Gen. 453 (2013) 34–44.
[40] A. Ota, M. Behrens, M. Armbruster, D. Rosenthal, M. Friedrich, I. Kasatkin, et al., Intermetallic Compound $Pd_2Ga$ as a Selective Catalyst for the Semi-Hydrogenation of Acetylene: From Model to High Performance Systems, 115 (2011) 1368–1374.
[41] S. Penner, B. Jenewein, K. Hayek, Pd–Al interaction at elevated temperatures: a TEM and SAED study, Catal. Lett. 113 (2007) 65–72.
[42] H. Park, J.H. Choi, K.M. Choi, D.K. Lee, J.K. Kang, Highly porous gallium oxide with a high $CO_2$ affinity for the photocatalytic conversion of carbon dioxide into methane, J. Mater. Chem. 22 (2012) 5304.
[43] S.E. Collins, M.A. Baltanás, A.L. Bonivardi, Infrared Spectroscopic Study of the Carbon Dioxide Adsorption on the Surface of $Ga_2O_3$ Polymorphs, J. Phys. Chem. B. 110 (2006) 5498–5507.
[44] Q. Liu, L. Wang, C. Wang, W. Qu, Z. Tian, H. Ma, et al., The effect of lanthanum doping on activity of Zn-Al spinel for transesterification, Appl. Catal. B Environ. 136-137 (2013) 210–217.
[45] G. Connell, The generation of Brønsted and Lewis acid sites on the surface of silica by addition of dopant cations, J. Catal. 105 (1987) 285–298.
[46] N. Cardona Martinez, Acid strength of silica-supported oxide catalysts studied by microcalorimetric measurements of pyridine adsorption, J. Catal. 127 (1991) 706–718.
[47] K. Kovnir, M. Schmidt, C. Waurisch, M. Armbruster, Y. Prots, Y. Grin, Refinement of the crystal structure of dipalladium gallium, $Pd_2Ga$, Z. Kristallogr. - New Cryst. Struct. 223 (2008) 7–8.
[48] F. Delbecq, Competitive C==C and C==O Adsorption of α-β-Unsaturated Aldehydes on Pt and Pd Surfaces in Relation with the Selectivity of Hydrogenation Reactions: A Theoretical Approach, J. Catal. 152 (1995) 217–236.
[49] V. Pallassana, Electronic Factors Governing Ethylene Hydrogenation and Dehydrogenation Activity of Pseudomorphic PdML/Re(0001), PdML/Ru(0001), Pd(111), and PdML/Au(111) Surfaces, J. Catal. 191 (2000) 301–317.
[50] J. Huang, T. Jiang, H. Gao, B. Han, Z. Liu, W. Wu, et al., Pd Nanoparticles Immobilized on Molecular Sieves by Ionic Liquids: Heterogeneous Catalysts for Solvent-Free Hydrogenation, Angew. Chem. 116 (2004) 1421–1423.
[51] M. Sahibzada, D. Chadwick, I.S. Metcalfe, Hydrogenation of carbon dioxide to methanol over palladium-promoted Cu/ZnO/$A1_2O_3$ catalysts, Catal. Today. 29 (1996) 367–372.
[52] F. Yaripour, F. Baghaei, I. Schmidt, J. Perregaard, Catalytic dehydration of methanol to dimethyl ether (DME) over solid-acid catalysts, Catal. Commun. 6 (2005) 147–152.
[53] M. Xu, J.H. Lunsford, D.W. Goodman, A. Bhattacharyya, Synthesis of dimethyl ether (DME) from methanol over solid-acid catalysts, Appl. Catal. Gen. 149 (1997) 289–301.
[54] C. Chang, The conversion of methanol and other O-compounds to hydrocarbons over zeolite catalysts, J. Catal. 47 (1977) 249–259.

[55] D. Barthomeuf, Zeolite acidity dependence on structure and chemical environment. Correlations with catalysis, Mater. Chem. Phys. 17 (1987) 49–71.
[56] P. Michorczyk, J. Ogonowski, Dehydrogenation of propane in the presence of carbon dioxide over oxide-based catalysts - Springer, REACT KINET CATAL L. 78 (2003) 41–47.
[57] M. Sayed, A Fourier-transform infrared spectral study of H-ZSM-5 surface sites and reactivity sequences in methanol conversion, J. Catal. 88 (1984) 137–149.
[58] H. Knozinger, Catalytical dehydration of aliphatic alcohols on gamma-$Al_2O_3$, J. Catal. 3 (1964) 559–560.
[59] H. Knozinger, Kinetics of the bimolecular ether formation from alcohols over alumina*1, J. Catal. 28 (1973) 69–75.
[60] E. Lalik, X. Liu, J. Klinowski, Role of gallium in the catalytic activity of zeolite [Si,Ga]-ZSM-5 for methanol conversion, J. Phys. Chem. 96 (1992) 805–809.
[61] M. Xu, J.H. Lunsford, D.W. Goodman, A. Bhattacharyya, Synthesis of dimethyl ether (DME) from methanol over solid-acid catalysts, Appl. Catal. Gen. 149 (1997) 289–301.
[62] F.S. Ramos, A.M.D. de Farias, L.E.P. Borges, J.L. Monteiro, M.A. Fraga, E.F. Sousa-Aguiar, et al., Role of dehydration catalyst acid properties on one-step DME synthesis over physical mixtures, Catal. Today. 101 (2005) 39–44.
[63] J. Datka, Acidic properties of supported niobium oxide catalysts: An infrared spectroscopy investigation, J. Catal. 135 (1992) 186–199.
[64] K. Tanabe, Catalytic application of niobium compounds, Catal. Today. 78 (2003) 65–77.
[65] J.-M. Jehng, I.E. Wachs, The molecular structures and reactivity of supported niobium oxide catalysts, Catal. Today. 8 (1990) 37–55.
[66] K. Tanabe, S. Okazaki, Various reactions catalyzed by niobium compounds and materials, Appl. Catal. Gen. 133 (1995) 191–218.
[67] T. Matsumoto, N. Sata, K. Kobayashi, Y. Yamabe-Mitarai, Surface Structures and Electrochemical Activity of Palladium-Niobium Binary Alloy Electrodes, and Glucose Biosensor with Palladium-Niobium Binary Alloy Electrode, Bull. Chem. Soc. Jpn. 86 (2013) 1317–1322.
[68] T. Ikeya, M. Senna, Change in the structure of niobium pentoxide due to mechanical and thermal treatments, J. Non-Cryst. Solids. 105 (1988) 243–250.
[69] B.X. Huang, K. Wang, J.S. Church, Y.-S. Li, Characterization of oxides on niobium by raman and infrared spectroscopy, Electrochimica Acta. 44 (1999) 2571–2577.
[70] S. Tamura, High-pressure phase research on $Nb_2O_5$, J. Mater. Sci. 7 (1972) 298–302.
[71] A.L. Viet, M.V. Reddy, R. Jose, B.V.R. Chowdari, S. Ramakrishna, Nanostructured $Nb_2O_5$ Polymorphs by Electrospinning for Rechargeable Lithium Batteries, J. Phys. Chem. C. 114 (2010) 664–671.
[72] A.A. McConnell, J.S. Aderson, C.N.R. Rao, Raman spectra of niobium oxides, Spectrochim. Acta Part Mol. Spectrosc. 32 (1976) 1067–1076.
[73] U. Balachandran, N.G. Eror, Raman spectrum of the high temperature form of $Nb_2O_5$, J. Mater. Sci. Lett. 1 (1982) 374–376.
[74] J.M. Jehng, I.E. Wachs, Structural chemistry and Raman spectra of niobium oxides, Chem. Mater. 3 (1991) 100–107.
[75] C. Nico, M.R.N. Soares, J. Rodrigues, M. Matos, R. Monteiro, M.P.F. Graça, et al., Sintered NbO Powders for Electronic Device Applications, J. Phys. Chem. C. 115 (2011) 4879–4886.

[76] J. Yoshihara, C.T. Campbell, Methanol Synthesis and Reverse Water–Gas Shift Kinetics over Cu(110) Model Catalysts: Structural Sensitivity, J. Catal. 161 (1996) 776–782.
[77] A. Goguet, F.C. Meunier, D. Tibiletti, J.P. Breen, R. Burch, Spectrokinetic Investigation of Reverse Water-Gas-Shift Reaction Intermediates over a Pt/$CeO_2$ Catalyst, J. Phys. Chem. B. 108 (2004) 20240–20246.
[78] W.-J. Shen, M. Okumura, Y. Matsumura, M. Haruta, The influence of the support on the activity and selectivity of Pd in CO hydrogenation, Appl. Catal. Gen. 213 (2001) 225–232.
[79] S. Ali, SSITKA Investigation of Palladium Precursor and Support Effects on CO Hydrogenation over Supported Pd Catalysts, J. Catal. 176 (1998) 3–13.
[80] P. Michorczyk, P. Kuśtrowski, A. Kolak, M. Zimowska, Ordered mesoporous $Ga_2O_3$ and $Ga_2O_3$–$Al_2O_3$ prepared by nanocasting as effective catalysts for propane dehydrogenation in the presence of $CO_2$, Catal. Commun. 35 (2013) 95–100.
[81] P. Michorczyk, P. Kuśtrowski, P. Niebrzydowska, A. Wach, Catalytic performance of sucrose-derived CMK-3 in oxidative dehydrogenation of propane to propene, Appl. Catal. Gen. 445-446 (2012) 321–328.
[82] American Chemical Society, ASTM Committee D-32 on Catalysts, American Chemical Society, Characterization and catalyst development: an interactive approach, American Chemical Society, Washington, DC, 1989.
[83] C.N. Satterfield, Heterogeneous catalysis in industrial practice, 2nd ed, Krieger Pub, Malabar, Fla, 1996.
[84] Introduction to zeolite science and practice, 2nd completely rev. and expanded ed, Elsevier, Amsterdam ; New York, 2001.

# Appendixes

**Appendix-A:** Reactor Design Parameters

For the design of the laboratory scale fixed bed reactor the following criteria were established:

i) Isobaric and Isothermal

ii) Ideal Flow

iii) Negligible concentration gradients

To get the ideal flow regime,we must meet the following conditions [82–84]:

i) The diameter of the reactor must be at least 10 times the diameter of the catalyst particle ($d_p$).

ii) The Reynolds number of the particle ($Re_p$) must be 10 or greater.

iii) $L/d_p > 50$, where L is the catalytic bed length.

**Appendix-B:** GC/MS Conditions (HP6890/HP5973)

-Carrier Gas:

He High Purity Grade (Praxair)

-Inlet:

Mode: Split

Temperature: 150 $^{o}$C

Pressure: 13.93 psi

Flow: 64.9 ml/min

-Column:

Model: J&W 19091-UO4 HP-PLOT/U

Dimensions: 30 m x 320 μm x 10 μm

Pressure: 13.93 psi

Flow: 3 ml/min

Average Velocity: 64 cm/s

-Oven:

Initial Temperature: 80 $^{o}$C

Hold Temperature: 80 $^{o}$C for 8 min

Ramp rate: 10 $^{o}$C/min f

Hold Temperature: 100 $^{o}$C for 2 min

**Appendix-C:** Accelerated Surface Area and Porosimetry Analyzer

-Degas Conditions (Physisorption and Chemisorption):

i) Evacuation Phase

Temperature Ramp Rate: 10 $^{o}$C/min

Target Temperature: 90 $^{o}$C

Evacuation Rate: 5 mmHg/s

Unrestricted evacuation from: 30 mmHg/s

Vacuum Setpoint: 20 μmHg/s

ii) Heating Phase

Ramp Rate: 10 $^{o}$C/min

Hold Temperature: 150 $^{o}$C

Hold Time: 300 min

iii) Evacuation and Heating Phases

Hold Pressure: 10 mmHg

- Chemisorption Pretreatment Conditions:

i) Reduction Phase

Ramp Rate: 5 $^{o}$C/min

Hold Temperature: 270 $^{o}$C

Hold Time: 120 min

ii) Evacuation Phase

Ramp Rate: 5 $^{o}$C/min

Hold Temperature: 270 $^{o}$C

Hold Time: 120 min

**Appendix-D:** FT-IR Parameters

-Number of Scans: 200

-Number of Background Scans: 200

-Resolution: 2

-Sample Gain: 8

-Optical Velocity: 1.8988

-Aperture: 34.00

-Detector: MCT or DTGS KBr

-Beam Splitter: XT-KBr

-Source: IR

**Appendix-E:** Number Acid Sites Calculations

The number of Lewis and Brønsted acid sites where calculated using the Beer-Lambert equation:

$$A = \frac{\varepsilon \,.\, W \,.\, Cw}{S}$$

where $A$ is the Absorption intensity (Area) [$cm^{-1}$], $\varepsilon$ is extinction coefficient [$m^2$/mol], $W$ is the sample weight [kg], $Cw$ is the Weight-based concentration [mol/kg], $S$ is the sample disk area [$m^2$].

The molar extinction coefficients used for the calculation of the Lewis and Brønsted acid sites were determined by Tamura and co-workers. The molar extinction coefficient corresponding to Lewis sites at 1440 $cm^{-1}$ and Brønsted sites at 1540 $cm^{-1}$ were 1.73 and 1.23 respectively.